UNIVERSITY OF SOUTHAMPTON

Converted PS-Wave Velocity Structure Of Post-Rift Sediments In the Eastern Black Sea

by
Georgios N. Moukos

A thesis submitted in partial fulfillment for the
degree of Master of Philosophy

in the
Faculty of Engineering, Science and Mathematics
School of Ocean & Earth Sciences

May 2014

Contents

List of Figure

List of Tables

Declaration

I, Georgios N.Moukos, declare that this thesis is the result of work done wholly or mainly by myself while in canditure for a research degree at the University of Southampton.

Acknowledgements

I would like to thank my parents, Kelly, my friends Vangelis, Klitos, Kakos and Melita for their never ending support and patience. I would also like to thank my supervisors Tim Minshull and Rose Edwards and everybody else I have met at NOC.

Summary

The combined analysis of P- and S-waves can be used successfully to characterize lithology and pore fluids, resolving ambiguities that would result from the analysis of P-wave data alone. Knowledge of S-wave velocity may also contribute to pore pressure estimation using either empirical relationships or rock physics models. Building on previously published P-wave velocity models and using travel-time forward modelling I have produced a two-dimensional S wave velocity model of the deep sediments of the Eastern Black Sea Basin (EBSB) using wide-angle seismic data collected in 2005. I model an approximately 100 km southeast-northwest transect in the eastern part of the EBSB, where 15 ocean bottom seismometers (OBS) were placed between the coast and the centre of the basin. Previous analysis has revealed a widespread low-velocity zone within the basin fill at depth 5-8.5 km, which I find is characterized by an S-wave velocity decrease from ~1.5 km/s to ~1.1 km/s. Using Differential Effective Medium Theory (DEM), a rock physics modeling approach, I interpret these velocities in terms of density and porosity variations within the basin fill. Porosity decreases from ~55% at seabed to ~2% at the top of the low velocity zone where it begins to increase and reach ~8% at the bottom of the sediments. The corresponding densities are ~1.8, ~2.58, and ~2.5 Mg/m^3 respectively. These values along with borehole measurements are used to calibrate the Eaton method, a pore pressure estimation technique which I used to estimate pore pressure. The results reveal a pore pressure variation from ~20 MPa at the sea floor (~2km below sea level) to ~200 MPa at the top of the Cretaceous (~9km below sea level).

Chapter 1: Introduction

1.0 Significance and Structure

Knowledge of pore pressure generation can lead to significant insights about tectonic mechanisms, the sedimentation rate and depositional history, diagenetic phenomena and fluid flow in a basin. Previous work in the Eastern Black Sea Basin (EBSB) (Scott *et al.*, 2009) based porosity and density analysis on empirical relationships and has not taken into account the aspect ratio of the sediment pores. In this dissertation I use Differential Effective Medium Theory (DEM) to relate porosity to seismic velocities and calibrate the exponent of the Eaton method to estimate pore pressures.

Chapter 1 of this thesis presents a theoretical background including: the geological setting and the timing and kinematics of the Black Sea opening, the main pore pressure generation mechanisms, uses for converted waves, pore pressure estimation by seismic velocities and DEM theory. The second chapter covers data acquisition and processing, while the third chapter presents the methods and the results of the S-wave analysis. In the fourth chapter I estimate the uncertainty of the model parameters. In the fifth chapter I present DEM modeling and results, and in the sixth chapter I estimate pore pressures. The seventh chapter is a discussion on the methods and the results obtained and finally in the eighth chapter I present the conclusions that I draw from my work.

1.1 Geological setting

The Black Sea is the world's largest land-locked inland sea. It is situated between $40^0$55' to 46^0 32' N and 27^0 27' to 41^0 32' E, covers an area of approximately 423,000 km^2, and has a present maximum and average bathymetry of 2200 and 1240 m, respectively (Meredith and Egan, 2002). To the west it is connected to the Mediterranean through the Bosporus (its only connection to the world's oceans), which is the narrowest strait in the world with an average width of 1.6 km, depth of 36 m and total length of 31 km. This restricted exchange with the oceans and the large fresh water input from major rivers such as the Dnieper and the Danube results in below normal salinity (Ross et al., 1978, Robinson et al., 1995b). To the north, the Black sea is connected with the Sea of Azov through the shallow Kerch Strait, which has depth of less than 20 m. Six countries located in Europe and Asia surround the Black sea: Bulgaria, Georgia, Romania, Russia, Turkey and Ukraine. Ninety per cent of its water mass is anoxic (Sorokin, 1983), so it contains the world's largest anoxic water mass (Bakan and Buyukgungor, 2000).

The tectonic setting of the Black Sea comprises many different geological formations (Figure 1.1). On the southern side of the Black sea there are the Pontides, which consist of the western Pontides whose basement is similar to the Precambrian Moesian Platform (Okay et al., 1994; Banks and Robinson, 1997; Nikishin *et al.*, 2003) the central Pontides, and the eastern Pontides with a Palaezoic basement (Okay and Sahinturk, 1997). Eastern of the Pontides there is the Achara-Trialet Zone and next to this Zone there is the Dzirula Massif whose prolongation within the Black Sea is the Shatsky High (Nikishin et al., 2003). On the southwest side of the basin there is

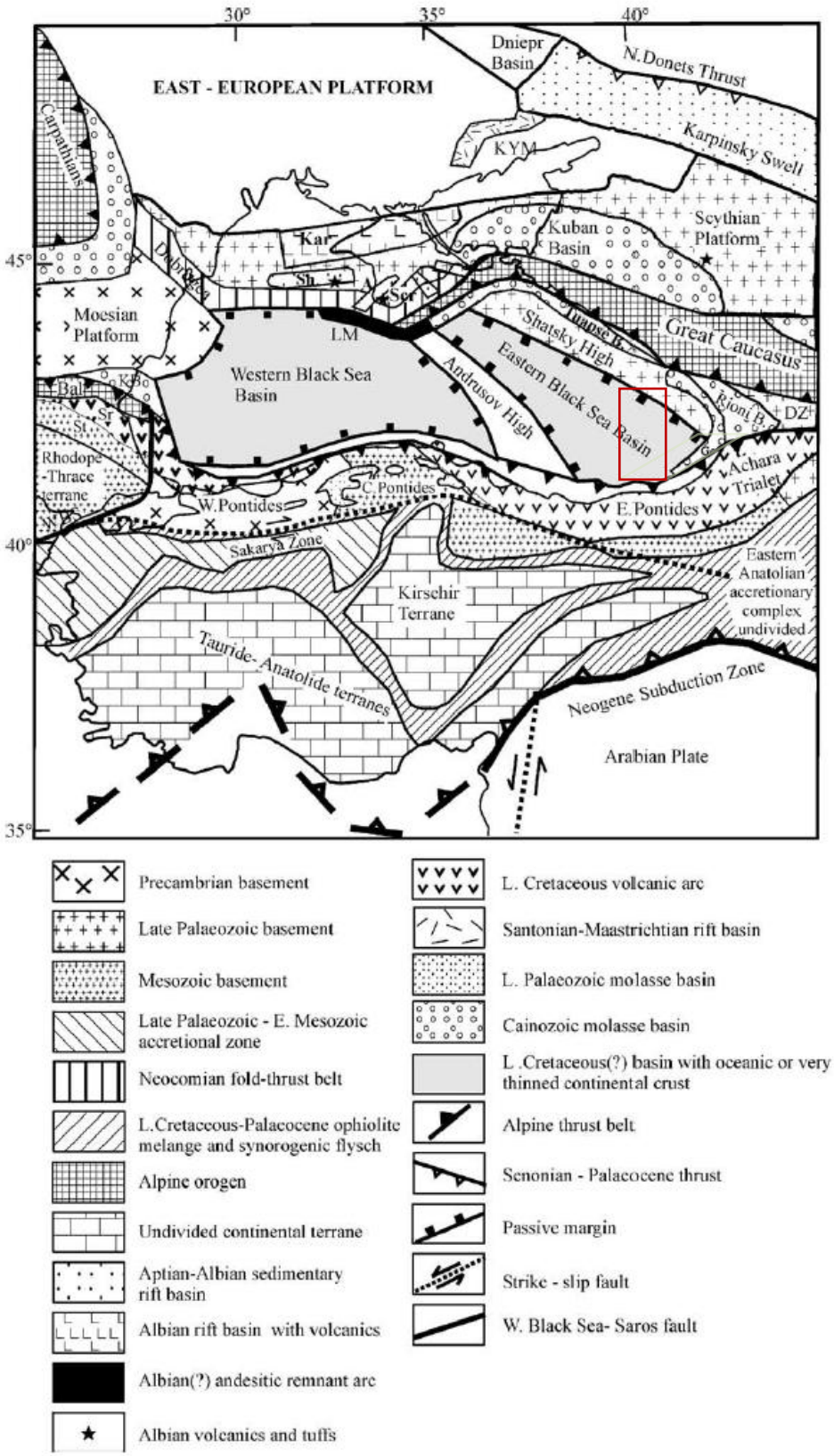

Figure 1.1: Tectonic setting of the Black Sea basin. Kar—Karkinit trough, Sh—Shtormovaya graben, A—Alma basin, Scr—Southern Crimea Orogen, Bal—Balkanides, K—Kamchia foreland basin, Sr—Srednogorie, St—Strandzha, WBS—West Black Sea – Saros Fault, Dz—Dzirula, G—Guriy basin, KYM—Konka – Yaly – Molochnaya graben.(from Nikishin *et al.*, 2003). The study area is indicated with the red box.

the Rhodope massif which consists of Palaeozoic and/or Precambrian basement (Burg et al.1996; Banks and Robinson, 1997, Nikishin et. al., 2002) and on the west there is the Moesian platform consisting of Late Precambrian basement affected by Late Variscan deformation (Okay et al, 1994; Banks, 1998). North of the Western Black Sea and next to the Moesian Platform there is the northern Dobrogea orogen which is consists of a former Permo-Triassic rift basin which from the time of the Jurassic/Cretaceous boundary underwent thrusting and folding up to the Neocomian times (Banks, 1998; Nikishin et al., 2001, 2002). On the northeast there is the Great Caucasus Alpine orogen which was created when a former Jurassic-Eocene back–arc basin was shortened and closed during Late Eocene to recent times (Milanovsky, 1991; Ershov et al., 1999, 2003; Nikishin et al., 1998, 2001, 2002). Northern of the Great Caucasus there is the Scythian Platform, which consists of Late Paleozoic basement deformed at the time of the Triassic/Jurassic boundary (Muratov, 1972; Milanovsky et al., 1992; Nikishin et al., 2001, Nikishin, 2003).

1.2 Timing and kinematics of the Black Sea opening

The Black Sea is generally considered to be a Cretaceous to Paleogene basin, which was formed in a back-arc extensional environment associated with the subduction of both the Paleo- and Neo-Tethys Oceans (Zonenshain and Lepichon, 1986; Gorur, 1988; Okay *et al.*, 1994; Robinson *et al.*, 1996; Nikishin et al., 1998, 2001). The basin comprises the Western and Eastern Black Sea sub-basins, which are separated by the Archangelsky and Adrusov ridges, collectively known as the Mid-Black Sea High which run SW-NE through the centre of the Black Sea (Figure 1.1). Although now they form one basin they have separate origins (Meredith and Egan, 2002). The older of the two basins, the Western Black Sea, rifted with dissection of the Moesian Platform of the northern supercontinent, Laurasia (Spadini et al., 1996).

The limestones of the Western Pontides are aged 130-125 Ma (Middle Barremian) (Inalte Formation) where they are unconformably overlain by Aptian to Albian synrift sediments including shallow water sandstones, submarine slides and olistostromes and turbidites (Spadini et al., 1996). Uncomformably overlying the syn-rift strata is a unit of pelagic carbonates and distal tuffs of Cenomanian age that is interpreted to mark the change from rift to drift in the Western Black Sea (Gorur et al.,1993). Analysis of seismic reflection data on the Romanian self shows tilted extensional fault blocks draped by chalks that can be dated as Cenomanian to Maastrichtian (Robinson et al., 1996). All the previous constraints suggest that rifting took place over a period of about 30 Myr with spreading occupying at most 6-7 Myr (Spadini et al., 1996).

The age of the rifting event in the Eastern Black Sea is not as well documented because relevant stratigraphy is poorly exposed. Modelling of seafloor heat flow measurements suggested that the basin is Jurassic in age (Golmshtok et al., 1992). The stratigraphy of the southern slopes of the Greater Caucasus in Russia and Georgia, where Sinemurian mudstones uncomformably overlie Hercynian metamorphic basement, demonstrates the presence of a Jurassic marine basin on the southern flank of the Russian platform. At least in the Middle Jurassic and late Cretaceous, this basin lay north of major volcanic arcs exposed now in the Eastern Pontides and can thus be considered to have formed in a back-arc setting (Robinson *et al.*, 1995a).

Three stratigraphic observations suggest rifting in the Eastern Black Sea in its present form took place after the Danian.

1) The northern rift shoulder of Shatsky ridge has been drilled and it appears to be a thick Mesozoic sequence which includes: Middle Jurassic volcanics and volcanoclastic sediments, Upper Jurassic to Lower Cretaceous limestones, and a

complete sequence of turbidites and chalks from Upper Cretaceous to Danian. These sediments are overlain uncomformably by Upper Eocene mudstones from (Robinson et al., 1996).

2) The same stratigraphic relationships are observed where the conjugate margin, the Archangelsky Ridge, outcrops at the seafloor (Rudat and MacGregor, 1993) .

3) The Upper Paleocene is missing in the Eastern Pontides (Robinson et al., 1995a). Dating of the deepest parts of post-rift fill suggests that spreading in the Eastern Black Sea was completed by the Middle Eocene (Robinson et al., 1996).

Beneath the Eastern Black Sea the Moho rises to about 25 km (Shillington et al., 2009). The base of the post-rift sediments is at a depth of ~10 km in the deepest parts of the basin and ~3.5 km at the edge of the MBSH (Scott et al., 2009). The lower crust in the area from onshore of Samsun until the centre of the eastern Black Sea basin has velocities which are too slow to correspond to gabbros, indicating that it is continental (Shillington et al., 2009). On the other hand crust from the eastern part of the basin is thicker with higher velocities that are best interpreted as either oceanic crust or synrift gabbros (Shillington et al., 2009).

By Neogene times these two sub-basins had coalesced to from the single basin structure present today. The Alpine-Himalayan orogenic belts that surround the Black Sea (including the Pontides, Greater Caucasus and Crimean Mountains) demonstrate that the evolution of the Black Sea region represents an interference of tectonic events over geological time in that most of the subsidence took place within the basin when the immediate surrounding regions were experiencing compressional deformation (Meredith and Egan, 2002).

1.3 Pore pressures

In general, pore pressures higher than normal (overpressures), are caused by the inability of pore-fluids to escape as the surrounding mineral matrix compacts under the lithostatic pressure caused by overlying layers (Swarbrick and Osborne, 1998). Many mechanisms have been proposed for the generation of overpressure in sedimentary basins. They can be divided into three main categories:

1) Increase in compressive stress, which is caused by tectonic compression and disequilibrium compaction.
2) Fluid volume change, which is caused by aquathermal expansion, mineral diagenesis and release of hydrocarbon from kerogen.
3) Fluid movement and processes related to density differences between fluids and gases, which are caused by hydraulic head, osmosis and buoyancy (Osborne and Swarbrick, 1997).

1.3.1. Increase in compressive stress

When burial in a sedimentary basin is slow then normal compaction of sediments occurs. This means that the equilibrium between overburden and reducing pore-fluid volume is maintained (Osborne and Swarbrick, 1997). However when the burial is rapid the increase of the overburden stress is also rapid. In order to maintain the equilibrium the fluids should be expelled fast. Where this does not happen the pressure of the pore fluids rises above hydrostatic values, a process that is called disequilibrium compaction. The depth beyond which fluids start to be retained by the sediment is called isolation depth. In theory, after this depth no fluid escapes, so the pore pressure rises along the pressure-depth path parallel to the lithostatic gradient (Osborne and Swarbrick, 1997). In reality, though, some fluid will continue to be expelled because permeability cannot have a value of zero. Disequilibrium

compaction is thought to be the main cause of overpressure in rapidly subsiding basins and it is the favored mechanism in a number of them such as the Gulf Coast (Dickinson, 1953), the Caspian Sea (Bredehoeft et al., 1988) and the North Sea (Mann and Mackenzie 1990; Audet and McConnell, 1992; Osborne and Swarbrick, 1997).

Disequilibrium compaction is not the only stress related mechanism that can cause overpressuring. Lateral compression can increase pore pressure in the same way as vertical stress (Osborne and Swarbrick, 1997). In fault zones that are susceptible to failure the overpressure build-up is very rapid and the pressure decrease can be equally fast if large volumes of fluid escape up the fault plane. This happens because the ductile creep makes the fault weak by leading to compaction that increases fluid pressure (Osborne and Swarbrick, 1997). Such a phenomenon can be avoided if the compression is so small that the rock neither buckles nor fractures. This way overpressure can be maintained over longer periods of time (Osborne and Swarbrick, 1997). Lateral compression is the characteristic mechanism for generating overpressures in accretionary wedges (Osborne and Swarbrick, 1997).

1.3.2. Change in volume

Aquathermal expansion is the process by which water will expand when heated. Aquathermal pressuring occurs in rock systems with very low permeability but is unlikely to be a major overpressuring mechanism (Osborne and Swarbrick, 1997). Sediment diagenesis often involves the release of bound water, such as the dehydration of smectite and gypsum to illite in clay rich mudrocks and to anhydrite in evaporites, respectively (Burst, 1969; Freed and Peacor, 1989). Smectite is a clay mineral that can hold a large amount of bound water. Assuming that the rock is initially 100% smectite and compacts normally , the overall increase in volume is a maximum of 4.0 vol% (Osborne and Swarbrick, 1997). Unless the rock is perfectly

sealed such a small increase in volume is unlikely to generate significant overpressures. The transformation of smectite to illite, though, also releases silica which reduces the permeability of shale and increases its ability to create a seal. So smectite dehydration may contribute to existing overpressures as a secondary mechanism but it is unlikely to be a primary cause of overpressure (Osborne and Swarbrick, 1997). The transformation from gypsum to anhydrite is a reaction controlled by temperature and the result is the loss of 39% bound water by volume. This is thought to be an important mechanism for generating overpressures in evaporite beds (Osborne and Swarbrick, 1997).

The top of overpressured zones often coincides with zones of hydrocarbon generation (Spencer, 1987). The kerogen maturation effect on fluid pressures is most pronounced when large volumes of liquid hydrocarbons are generated within a short period of time in low-permeability rocks, and where primarily migration is difficult (Osborne and Swarbrick, 1997). The distribution of overpressure in hydrocarbon basins reflects the depth, temperature and location of the source rocks with the necessary maturation levels to be producing gas (Swarbrick and Osborne, 1998). As well as the volume expansion, the presence of oil and gas as separate phases to water acts to reduce the permeability of fine-grained rocks, thus helping to seal overpressures.

1.3.3. Fluid movement and buoyancy

Marine and Fritz (1981) proposed as a mechanism for overpressure, under certain conditions, the fluid transfer across a semipermeable membrane due to osmosis, induced by large contrast in the salinity of pore fluids. The required conditions are that the rock must be a near perfect membrane, have no micro-fractures and the water, fresh and brine, must be recharged to maintain the salinity contrast.

Nevertheless often in overpressured zones the pore fluid has lower salinity than in normal pressured zones. This would have the opposite effect and actually reduce the pressure (Osborne and Swarbrick, 1997).

All gases that are formed through hydrocarbon maturation have a lower density than pore water. As a gas bubble rises because of buoyancy, it will expand because of the pressure decrease. If the system is completely sealed, the pore fluids are incompressible and the bubble will not be able to expand, so the overpressure will increase (Osborne and Swarbrick, 1997). This mechanism is a secondary method for the creating of overpressure.

Potentiometric or hydraulic head form the mechanism that exerts a pressure in the subsurface when the water table in highland areas is elevated and the aquifer or reservoir is sealed from above. It is measured as the vertical height of the highland water table above the level of the sea and is often called "equilibrium overpressure" (Neuzil, 1995). The reservoir beneath the seal must be laterally continuous over long distances in order for this mechanism to create a substantial overpressure. However even when this happens in basins like the central United States Basin and Range province the amount of overpressure cannot exceed the height of the elevated water table (Osborne and Swarbrick, 1997).

1.4 Converted waves

The term "converted wave" describes a downgoing P-wave that converts on reflection to an upcoming S-wave. This kind of seismic wave is increasingly used to explore subsurface targets. Applications that have arisen include imaging, lithological estimation, anisotropy analysis, subsurface fluid description and reservoir monitoring (Stewart et al., 2003).

1. Imaging:

i) *"Seeing" through gas-charged sediments*: P-wave energy is delayed, scattered and attenuated when passing through a gas bearing sediment. S-waves, being generally less sensitive to rock saturants, can be used to penetrate gas-saturated sediments. For example Granli et al. (1999) using OBS with three component geophones planted on the ocean bottom were able to image through a gas chimney at the Tommeliten Alpha field. Li et al. (2001) analyzed a four-component data set from Valhall field, Norway. They noted focused and continuous reflectors by using prestack versus poststack P-S migrations and they concluded that the images taken from this method are better than with P-P methods.

ii) *Structural imaging:* Resolution of steeply dipping features can be improved using converted waves in certain circumstances. Purnell (1992) presented examples where high dip anomalies were more visible on migrated P-S data than P-P.

2. *Near-surface imaging:* P-S sections provide more highly resolved reflectors in the near-surface than P-P sections. This is the result of several factors, including greater relative changes in S versus P velocity, a greater impact of density changes on the P-S reflectivity than on P-P or even a shorter S wavelength.

3. Lithology Estimation :

S-wave measurements provide constraints on the rock properties, especially on density and rigidity contrasts. Much P-S analysis is targeted at finding an S-wave velocity or determining a V_p/V_s value (or Poisson's ratio) because both can be good indicators of rock type.

4. Anisotropy Analysis :

   Evaluating and accounting for elastic anisotropy can improve seismic imaging of the subsurface through more accurate velocity analysis. Understanding the influence of elastic anisotropy is particularly important in the P-S processes because shear polarizations are generally more strongly affected than compressional polarizations (Haacke and Westbrook, 2006).

5. Fluid Description

   Berryman et al. (2002) were able to estimate fluid saturation magnitudes and spatial distribution as well as porosity using only P and P-S velocities. The key idea was that the density and the Lame elastic parameter λ are the only two parameters determining seismic velocities that also contain information about fluid saturation. At low frequencies, Gassman's equations show that shear modulus is independent of the fluid saturation level. They used these insights to construct saturation-proxy and data sorting plots from seismic velocity data.

6. Reservoir Monitoring

   There are variations in the reservoir rock properties associated with temperature and saturation changes. These, in return, are associated with changes in the seismic character of both P-P and P-S sections (Stewart et al., 2003).

1.5 Predicting abnormal pressures using seismic velocities

1.5.1 Pressure concepts

Pore pressure P_f is defined as the in situ pressure of the fluids in the pore spaces of a sedimentary rock. The hydrostatic pressure P_{hf} is the pressure exerted by the weight of a static column of seawater and is equal to:

$$P_{hf}(z) = \rho_w g z \quad (1)$$

where z is the height of the fluid column and ρ_w is the fluid density. When the pore fluids only support the weight of the overlying pore fluids, the pore pressure and hydrostatic pressure are equal. The lithostatic or confining pressure or total pressure in the vertical direction σ_v is due to the weight of the overlying sediments, including the pore fluids. Therefore confining stress is equal to:

$$\sigma_v = g \int_0^z \rho(z')dz' \quad (2)$$

where ρ is the wet bulk density, including seawater above the seafloor, g is the gravitational acceleration and z is depth. In the absence of any state of stress in rock, the pore pressure attains hydrostatic pressure and the fluids support all the weight. However, fractures appear perpendicular to the direction of the minimum compressive stress when pore pressures reach 70-90% of the confining pressure. In this case, the fluid escapes from the pores and pore pressure decreases. A rock is said to be overpressured when its pore pressure is significantly greater than hydrostatic pressure. The difference between confining pressure and pore pressure is called differential pressure. For the evaluation of the degree of overpressure in comparison to the hydrostatic effective pressure (the difference between confining pressure and hydrostatic pore pressure) the normalized pore pressure ratio λ^* is defined:

$$\lambda^* = \frac{P_f - P_{hf}}{\sigma_v - P_{hf}} \quad (3)$$

1.5.2 Pressure-velocity regimes

Hydrocarbon reservoirs are generally overpressured. This situation can, in principle, be characterized by seismic waves. To do this, the dependence of the P-wave and S-wave velocities on effective stress plays an important role (Carcione and Helle, 2002). Many previous studies of overpressure prediction from seismic interval velocities have relied on empirical relationships (e.g., Han and Nur, 1986; Eberhart-Phillips, 1989; Eaton, 1976; Dutta, 2002; Han, 1986). Pore pressure estimation is easily done if the sedimentary sequence is stratified and many boreholes penetrate it, by comparing an abnormal compaction trend with a normal compaction trend assuming a compaction disequilibrium regime (e.g. Hubbert and Rubey, 1959; Eaton, 1972). However in some cases, such as this study, it is difficult to define appropriate compaction trends. Then there is a need to predict pore pressure using an estimated relationship between velocity and effective stress. Alternatively one could predict effective stress and pore fluid pressure by applying rock physics theory to observed seismic interval velocities (Tsuji et al., 2008).

Many theoretical models have been proposed that attempt to establish a link between formation parameters and seismic velocities (e.g., Mavko et al., 1998). The relationship between effective stress and seismic velocity depends on pore volume, pore shape, mineral texture and mineral composition (Schon, 1996). Total porosity (pore volume) is one of the most important parameters of those that determine velocities (e.g., Hyndman and Spence, 1992). However, pore shape (crack or void) also significantly influences seismic velocity, independent of total porosity. Because thin cracks with small pore volume can significantly decrease velocities (Kuster and Toksoz, 1974), pore features need to be taken into consideration as well as total

porosity. To construct velocity-stress relationships that can be used to predict pore pressures therefore I consider pore geometries (e.g., aspect ratio) (Figure 1.2).

For unconsolidated shallow sedimentary sequences close to the seafloor, seismic velocities increase with effective stress as a result of the strengthening of grain contacts as effective stress increases (Mindlin, 1949, Dvorkin and Nur, 1996). In consolidated rocks, closure of cracks in the rock in response to increasing effective stress is the main influence on velocity (e.g. Kuster and Toksoz, 1974; Carcione et al., 2003; Tsuji et al., 2008).

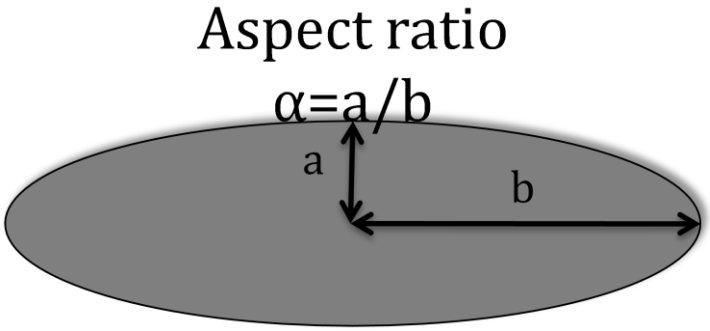

Figure 1.2: Aspect ratio description of ellipsoidal pores. It is easy to understand from aspect ratio's definition that when α approaches 1 the pores will be spheres and when it approaches 0 they will be thin cracks.

1.5.3 The Eaton method

The Eaton method, as described by den Boer et al. (2006) directly relates effective stress to the ratio of the observed seismic velocities (V_{obs}) to the velocity in normally pressurized sediments (V_{norm}), where pore pressure (P_p) is equal to the hydrostatic pressure (P_{hf}). The method is described by the following equation:

$$P_p=L_p-(L_p-P_{hf})(V_{obs}/V_{norm})^n \quad (4)$$

where the exponent n is used to control the sensitivity of seismic velocity to changes in effective stress and L_p is the lithostatic pressure. The equations implies that if $V_{obs}= V_{norm}$ the rock is normally compacted and $P_p= P_{hf}$. Conversely, if the measured velocity is smaller than the normal velocity i.e. $V_{obs} < V_{norm}$, $P_p>P_{hf}$ and the rock is

overpressured. The limitations of the Eaton method are that it is applicable to overpressure due to undercompaction of shale, which occurs during monotonic overburden stress increase due to burial and the fact that the exponent n of equation 4 is highly site specific and requires thorough calibration (Mavko *et al.*, 2003).

1.6 Differential effective medium theory

Differential effective medium theory, or DEM, was developed by Bruggeman (1935) and Roscoe (1952) for classical percolation and conduction problems. In DEM theory a physical parameter is estimated by successively computing the change in the effective constants after infinitesimal amounts of the inclusion phase are added to a homogeneous material whose effective constants are the same as those computed for the composite up to the current volume fraction (Berryman, 1992). DEM is necessarily asymmetric because the medium used to start the imbedding process (called host) is always continuous (Yonezawa and Cohen, 1983, Berryman, 1992). McLaughlin (1977) showed that the DEM satisfies the Hashin-Shtrikman bounds, which are for the bulk and shear modulus:

$$K^{HS\pm} = K_1 + \frac{f_2}{(K_2 - K_1)^{-1} + f_1\left(K_1 + \frac{4}{3}\mu_1\right)^{-1}}$$

$$\mu^{HS\pm} = \mu_1 + \frac{f_2}{(\mu_2 - \mu_1)^{-1} + 2f_1(K_1 + 2\mu_1)/[5\mu_1\left(K_1 + \frac{4}{3}\mu_1\right)]} \quad (5)$$

Where K_1 and K_2 are the bulk moduli of individual phases;μ_1 and μ_2 are the shear moduli of individual phases; and f_1 and f_2 are the volume fractions of individual phases. Upper and lower bounds are computed by interchanging which material is

termed 1 and which is termed 2. The expressions yield the upper bound when the stiffest material is termed 1 and the lower bound when the softest material is termed 2 (Mavko et al., 2003). Many authors (Milton, 1985, Norris et al., 1985, Norris, 1985, Avellaneda, 1987), have shown that the DEM is also a realizable model (Berryman, 1992).

The coupled differential equations for the effective bulk and shear moduli K* and μ*, respectively, are (Berryman, 1992, Berryman and Berge, 1993, Berge et al., 1993, Mukerji et al., 1995):

$$(1-y)\frac{d}{dy}[K^*(y)] = (K_2 - K^*)P^{(*2)}(y)$$
$$(1-y)\frac{d}{dy}[\mu^*(y)] = (\mu_2 - \mu^*)Q^{(*2)}(y) \quad (6)$$

with initial conditions $K^*(0)=K_1$ and $\mu^*(0)=\mu_1$, where K_1 and μ_1 are the bulk and shear moduli of the pure initial host material (phase 1), K_2 and μ_2 are the moduli of the other end member (the incrementally added inclusion phase, phase 2), and y is the concentration of phase 2. For fluid inclusions and voids, y=φ, the porosity. The factors $P^{(*2)}$ and $Q^{(*2)}$ depend on the shape of the inclusions (i.e., ellipsoid aspect ratio α), and are functions of the effective moduli and the moduli of phase 2.

In the usual DEM model, starting from a solid initial host, a porous material stays intact at all porosities and only falls apart at the very end when y=1 (100 percent porosity). This is because the solid host remains connected and therefore load bearing. From the equations for K* and μ* we see that as $\rightarrow 1$, the left hand side goes to zero; to satisfy the equation, on the right hand side, $K^* \rightarrow K_2$ and $\mu^* \rightarrow \mu_2$. (For dry porous materials $\mu_2=0$ and $K_2 \cong 0$). The point (K_2, μ_2) is sometimes called the attractor. From any initial (K_1, μ_1) at y=0, the solution always tends to (K_2, μ_2) as $y \rightarrow 1$ (Mukerji et al., 1995).

1.6.1 Assumptions and limitations of DEM theory

DEM theory assumes that the rock is isotropic, linear and elastic. It also assumes idealized ellipsoidal inclusion shapes. Cracks are assumed to be isolated with respect to fluid flow. Pore pressures are unequilibrated and adiabatic. The process of incrementally adding inclusions to the matrix is a thought experiment and should not be taken to provide an accurate description of the true evolution of rock porosity in nature (Mavko et al., 1998).

Chapter 2: Data acquisition and processing

2.1 Wide-angle data collection

The wide-angle seismic data were acquired as part of the research project "Integrated seismic and subsidence study of conjugate margin systems in the eastern Black Sea Basin". The project was funded through the UK Ocean Margins LINK Program, by the UK Natural Environment Research Council (NERC), BP Turkey and TPAO (Turkish state oil company). The experiment took place during February and March of 2005, onboard the RV Iskatel. Four profiles were acquired, located near-coincident to existing normal-incidence multichannel seismic (MCS) lines. The first profile (Line 1) is margin-parallel, orientated southeast-northwest constraining some of the thinnest crust within the basin. The other three profiles (Lines 2, 3 and 4) are orientated southwest-northeast, and constrain the extension of the rift from the coast to the centre of the basin. The layout of the survey, and positions relative to the existing MCS profiles is shown in Figure 2.1.

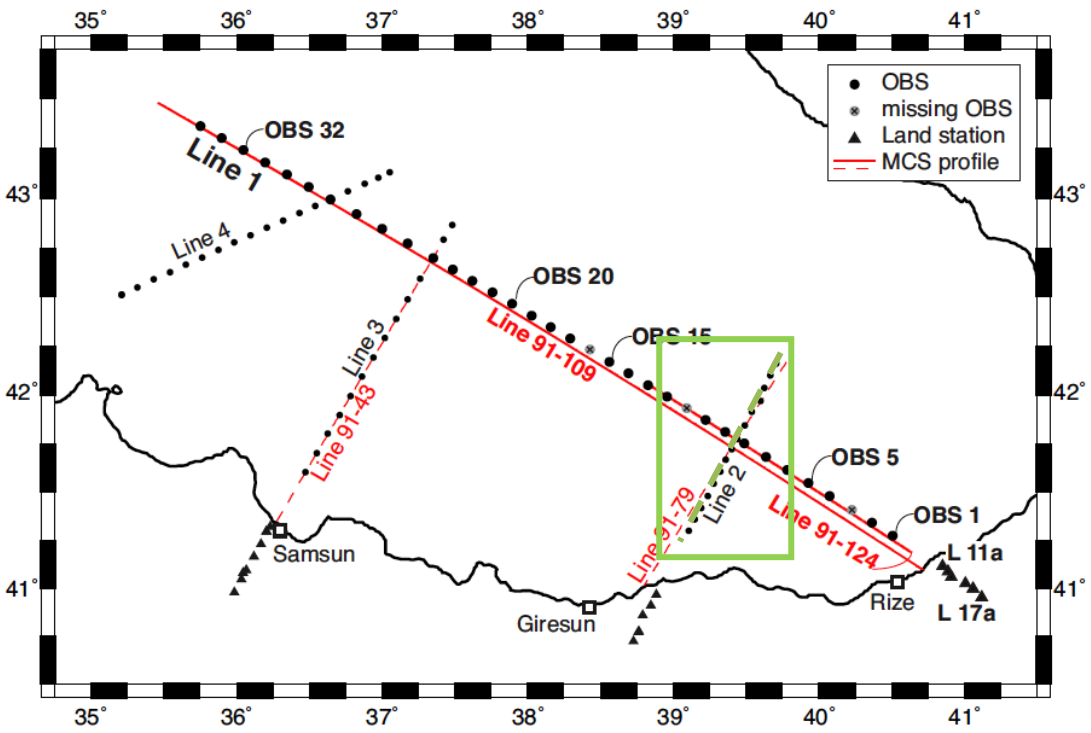

Figure 2.1: Plot of the wide angle seismic profiles acquired in the EBS with existing MCS profiles. Black dots represent OBS locations, black triangle represent land stations, the red lines indicate the location of near-coincident, normal incidence MCS reflection profiles that are used in combination with the wide-angle data to produce seismic velocity models. The three OBS that were lost or failed to with. (Scott, 2008).

The seismic source consisted of nine Bolt Long Life airguns towed at a depth of 9 m. The airguns were clustered so that their bubbles coalesced, and the total source volume was 3140 cu.in, rich in low frequencies. The array consisted of 3 x 500 cu.in, 4 x 310 cu. in and 2 x 200 cu. in guns. Shots were triggered every 60 s or 90 s from a stable clock that was accurate to within under 1 ms and was synchronised with onboard Global Positioning System (GPS). The layout of the airguns and relationship to the GPS systems is shown in Fig. 2.2.

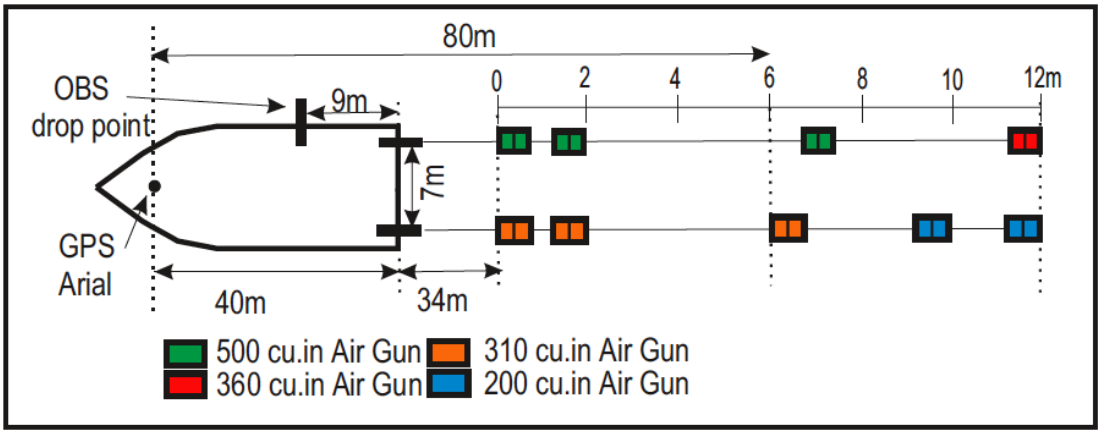

Figure 2.2: A schematic drawing showing the layout of the airgun source array, with respect to GPS receivers located on board (Scott, 2008).

Air-gun shots were recorded on ocean bottom seismometers (OBS) and land seismometers, which extended each profile onshore (Figure 2.1). GeoPro GmbH provided the OBS, which are housed in a 17" Benthos glass sphere, attached to an anchor for deployment and released by radio transmission for recovery. Each unit contains a data logger operating at a 4 ms sample rate, a Benthos hydrophone and a three-component 4.5 Hz seismometer, housed at the base of the sphere. The OBS were deployed and recovered by GeoPro GmbH crew. Of the 78 instruments that were deployed, two instruments were lost. This dissertation focuses on Line 2 which is ~100km long with a total of 15 Ocean Bottom Seismometer (OBS) instruments spaced ~7km which crossed the most south-easterly section of the basin in a North-East – South-West orientation. Line 2 was shot from offshore Giresun (41^{o}N 39^{o}E) to the centre of the Eastern Black Sea Basin, crossing the most easterly part of the basin, parallel to Line 3. Conditions during the shooting of Line 2 were good, and data quality along this line is excellent (Figure 2.3) (Scott, 2008).

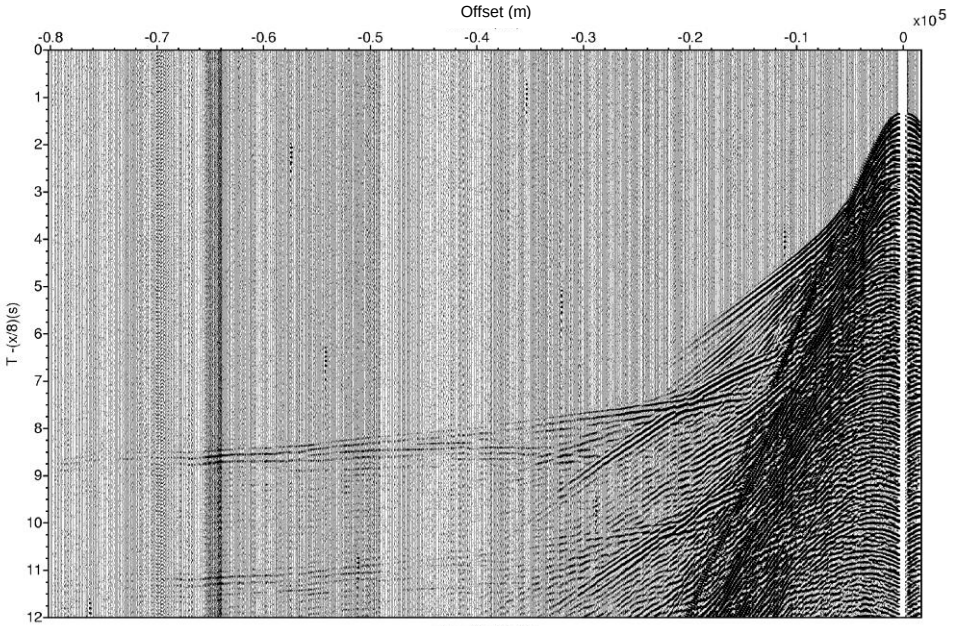

Line 2, OBS1

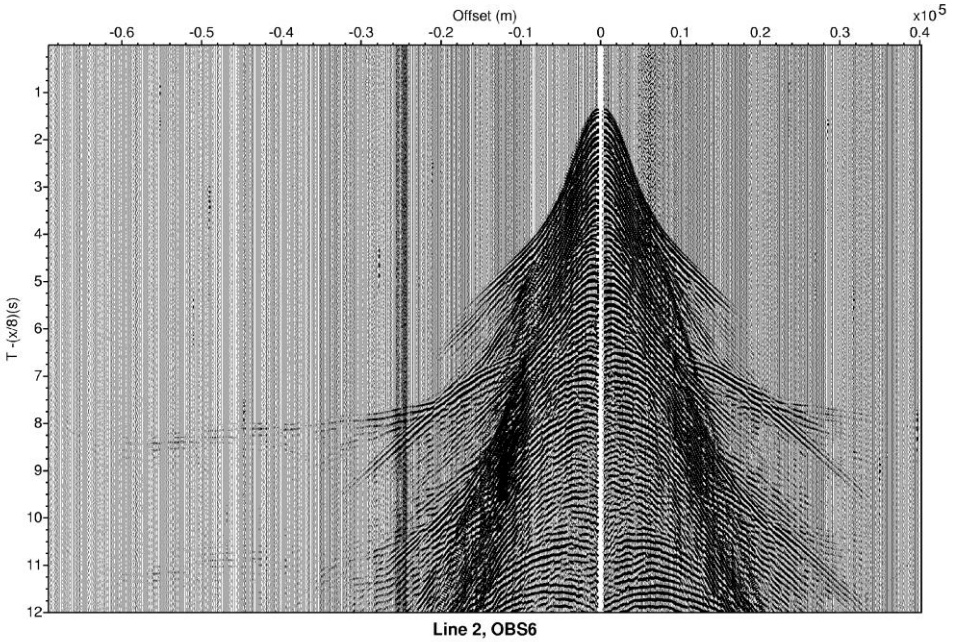

Line 2, OBS6

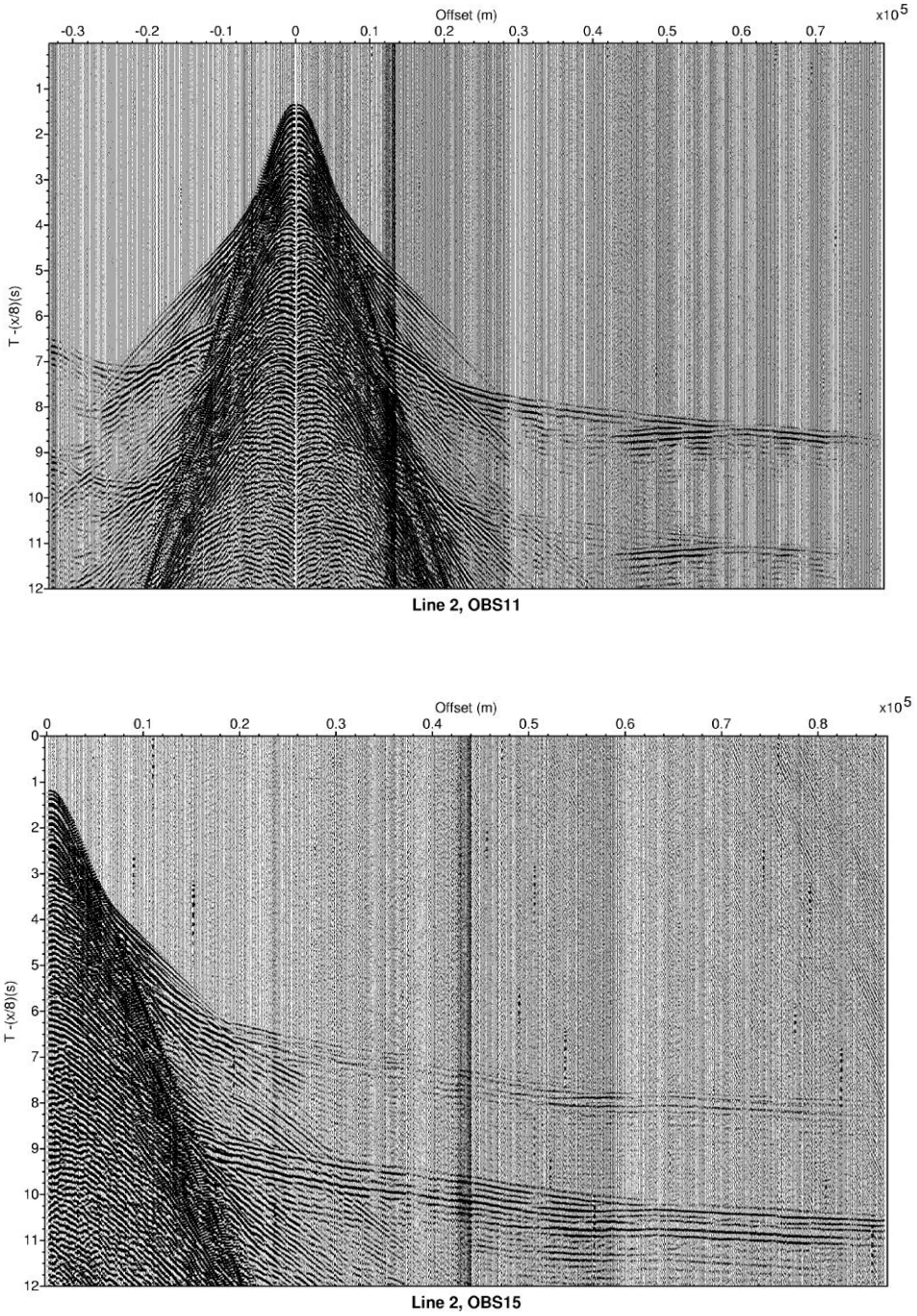

Figure 2.3: Record section of the vertical geophone of OBS 1,6,11 and 15 on Line 2. The plot has been filtered using a minimum-phase filter with corner frequencies of 3-5-17-21 Hz. The sections are plotted with a reduction velocity (linear moveout) of 8km/s.

2.2 Travel-time modelling

The models that we describe in the following chapter were generated using the forward/inverse modelling code rayinvr of Zelt and Smith (1992). RAYINVR is a popular code that uses a layer-stripping approach, modelling from the top down. The model is defined as a series of depth and velocity nodes that can have irregular spacing, and any or all model parameters may be inverted at any time. Ray tracing is performed by numerically solving the ray trace equations for 2D media using a Runge-Kutta method, and all seismic arrival types can be modelled (Zelt and Smith, 1992). The source and receiver locations are set as input parameters, and traveltimes are calculated by numerical intergration along the ray paths. Using an initial 2D model RAYINVR traces rays from each source though the model. Ray take-off angles are automatically determined for ray groups that are specified by the user. The program then calculates a χ^2 error value that has the form

$$\chi^2 = \frac{1}{n_{res}} \sum_{j=1}^{n_{res}} \left(\frac{r_j}{\sigma_j} \right)^2 \tag{7}$$

where r_j is the element of the traveltime residual vector **r** corresponding to the jth traveltime datum, and σ_j is the picking error associated with that traveltime. It represents the difference between calculated traveltimes and the observed data picks weighted by their assigned error. A χ^2 of 1 describes a model that fits exactly to the assigned uncertainties while $\chi^2 >> 1$ describes a poor fit to the data and $\chi^2 < 1$ suggests that the model has been over-fit to the data. A normalized misfit of $\chi^2 < 1.05$ was achieved for the vast majority of the models presented here.

Chapter 3: Methods and results

Many publications that use OBS data to estimate P-S wave velocity and Poisson's ratios (σ) (e.g. Bunz et al., 2005; Wang and Pan, 2001) rely on a fine-tuned P-wave velocity-depth model, which includes P-wave reflections. Typically either all or the majority of the P-wave reflections are used for the P-S wave model as well and the P-wave velocity (u_p) is kept fixed so that only σ is perturbed to model S-wave velocities. In our case the P-wave velocity-depth model presented by Scott et al. (2009) includes only three reflections above basement (and two refractions that will not be used) (Figure 3.1), a number that is not enough to draw conclusions for the changes in σ or the estimation of porosities and pore pressures.

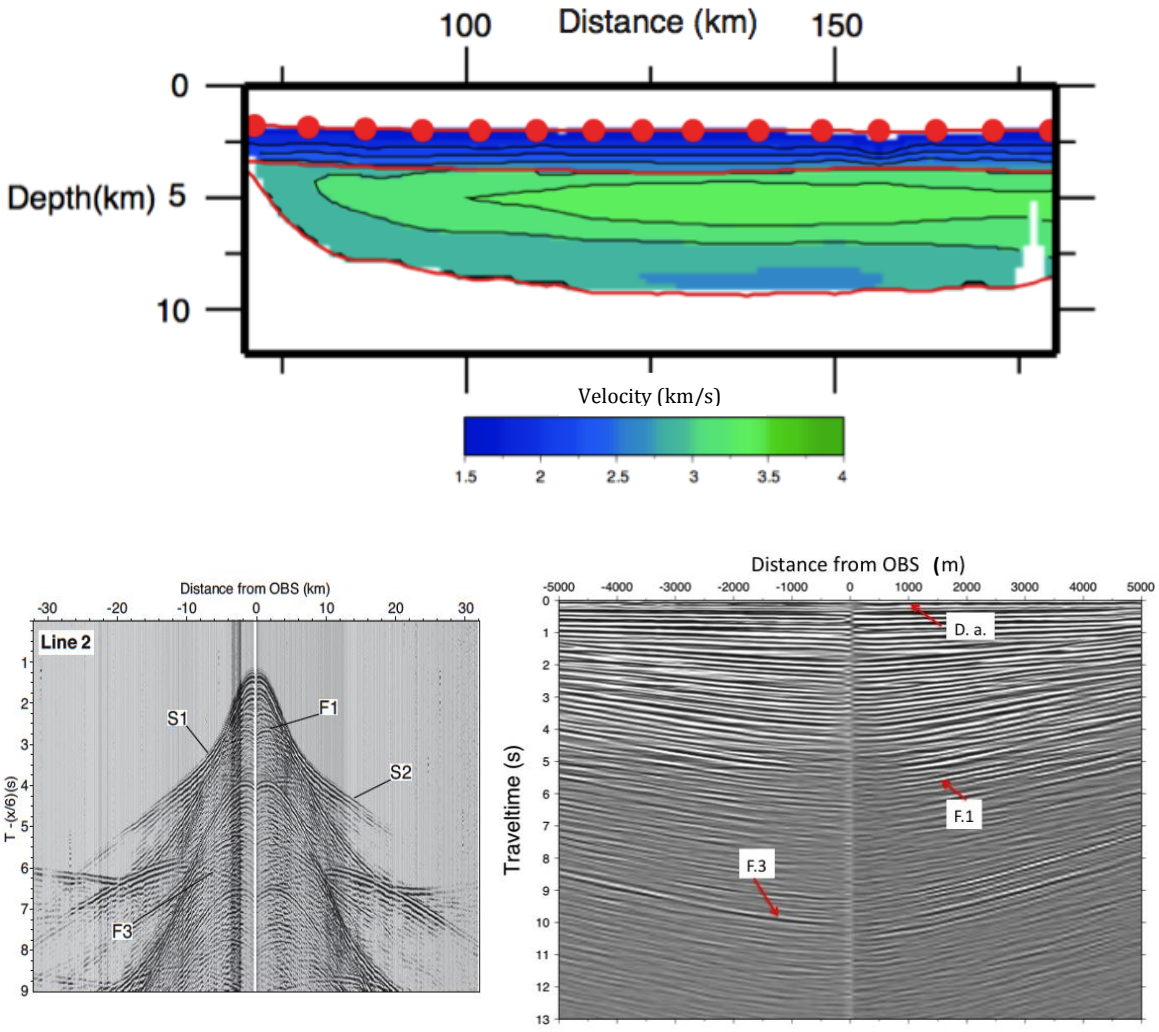

Figure 3.1: (Top picture) P-wave velocity-depth model of Line 2 (Scott et al., 2009). The red dots show the positions of the OBS and the red lines are the reflections used. From top to bottom we can see the sea bed, the first reflection which is a shallow sendimentary reflection and the top of the acoustic basement.(Lower left picture) P-wave reflection and refractions picked to produce the above velocity model shown in OBS 12. F1 and F3 are the reflections and S1 and S3 the refractions.(Lower right picture). Data from the radial componet of the same OBS flattened at the direct arrival (D.a.) showing the S-wave reflections corresponding to F.1 and F.3 that I used to produce the S-wave velocity model of Figure 3.2.

The first reflection modelled is the reflection of the seabed; the second is a shallow reflection at ~3.5 km depth corresponding to a change in the apparent velocity gradient between the two refracted phases. The third reflection is the acoustic basement and the base of my velocity model. It was relatively easy to produce a P-S wave velocity-depth model using these reflections. The descending P-wave is reflected and part of it converts to an ascending S-wave at these reflections. I picked

traveltimes at the exact zero crossing point using the radial component of each OBS. I set up an 1-D P-wave velocity-depth model for each OBS using Scott et al.'s, (2009) model so the only value I had to perturb was σ. Then I picked traveltimesfrom many horizons and tried to see which is the one that fits the model the best. Many of these horizons were within the margin of error but the events having the least residual were picked. The model showed that the first layer, between the seabed and shallow reflection, has a value of σ with the best fit to the model σ =0.438 and the second layer has σ =0.372. The corresponding S wave model is presented in Figure 3.2.

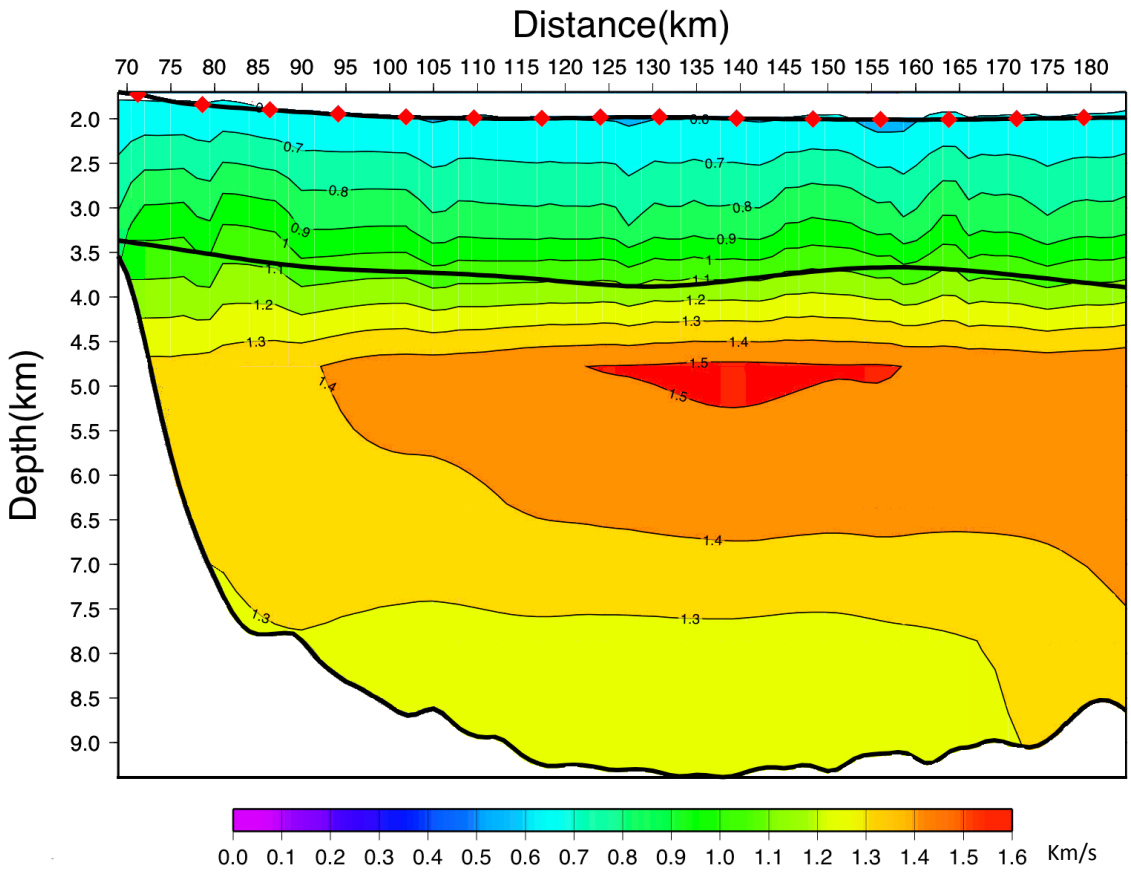

Figure 3.2: S wave velocity-depth model of Line 2 using only reflections from Scott et al. (2009) and interpolation of 1D models. The red diamonds are the OBS, the black line is the middle is the shallow sedimentary reflection F.1, and the white part represents the acoustic basement.

In order to implement a non-empirical method to estimate pore pressures a more detailed model is needed than the one in Figure 3.2. That meant that I had to model more sedimentary reflections. To do so I systematically identified reflections which

could be found on all OBS. A typical RAYINVR plot of the reflections and the residuals of each reflection can be seen in Figure 3.3. I found 4 reflections that were strong on every OBS and these, with the direct arrival and the acoustic basement, are marked on the record section of OBS 8 in Figure 3.4.

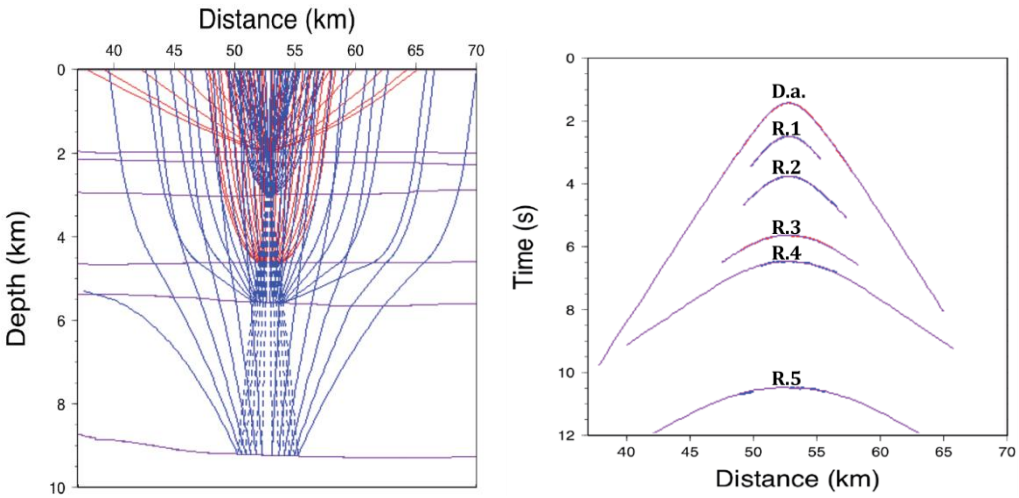

Figure 3.3: S-wave velocity model of OBS 8 and the residuals of each reflection. We used 576 data points for this model and the RMS traveltime residuals is 10 ms. In the picture on the left we can see the P-waves descending (solid lines) and converting into ascending S-waves(dashed lines). As we can see from the plot on the right the model fits the data very well.

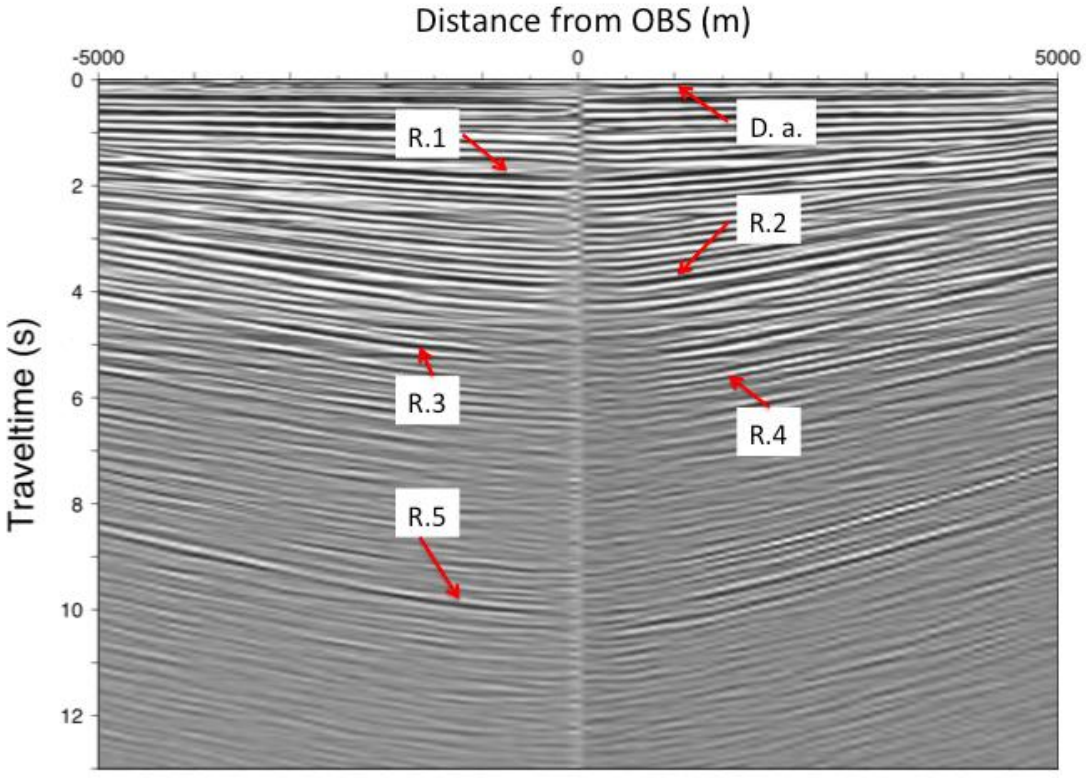

Figure 3.4: OBS 8 radial component flattened on the direct arrival with the S wave reflections that produced the model marked on it. D.a. denotes the direct arrival and R.1,2,3…5 denote the first ,second…fifth P-S transforming reflection. D.a. and R.5 were the reflections used by Scott et al.(2009). R.4 coincides with the top of the low velocity zone and R.5 is the top of the acoustic basement.

The errors assigned were 10 ms for the direct arrival and 15 ms for all the other reflections. The residuals of the entire best-fitting model were ~13 ms for the majority of the OBS. After having modelled every OBS I created a 2-D model for Line 2 combining all the individual models of each OBS with just small modifications needed. This model has the direct arrival and five reflections: two shallow sedimentary reflections at ~250 m, ~ 1km, below the seabed, two deeper sedimentary reflections at ~2.5 km and 3.5 km below the seabed and the reflection of the acoustic basement. The best-fitting value of σ varies between 0.378 and 0.485 (Table 1).

Layer	Poisson's Ratio σ	Depth (km)	RMS residual (ms)	Number of picks
1	0.485	~0.25	10	~100
2	0.406	~1	15	~90
3	0.386	~2.5	15	~80
4	0.378	~3.5	15	~80
5	0.417	~8.5	13	~70

Table 1: Values of σ, approximate depth below seabed and RMS residuals of every layer of the model.

In the following figures we present the results of the model. σ in the first four layers decreases as the depth increases, as expected since the deeper a sediment is the more consolidated it is and the higher the velocity becomes. In the fifth layer, though, there is an increase in σ from 0.376 to 0.417. The last layer was expected to present an increase in σ since it coincides with the Maikop formation as identified from the work that Scott et al.,2009 has done, where the P-wave velocity decreases and the sediments are generally overpressured (Scott et al., 2009)(Figures 3.5 and 3.7).

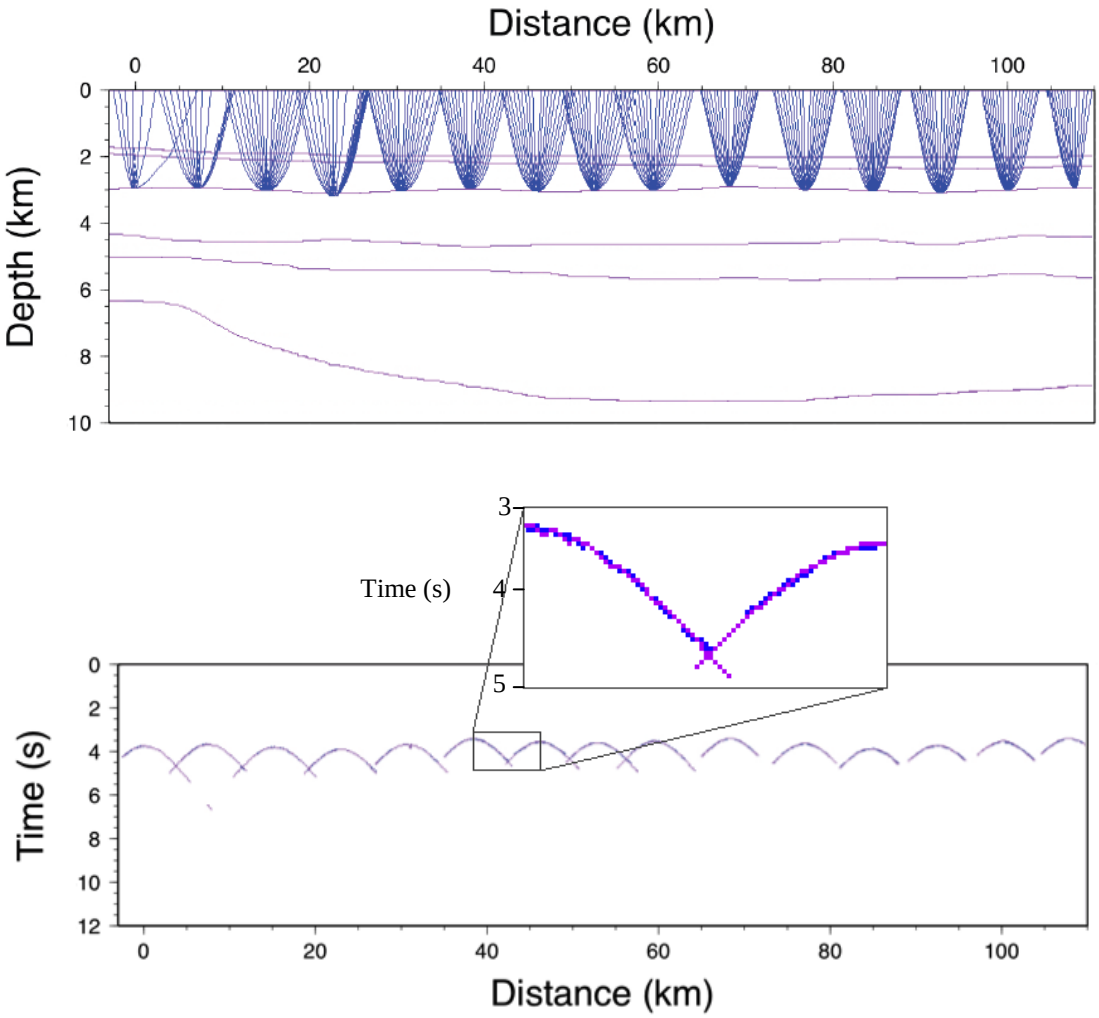

Figure 3.5: RAYINVR plot of layer 2 (top) of the 2-D model and its residuals (bottom). The zoom in part of the bottom picture shows as how well the data (blue spots) fit the model (purple line).

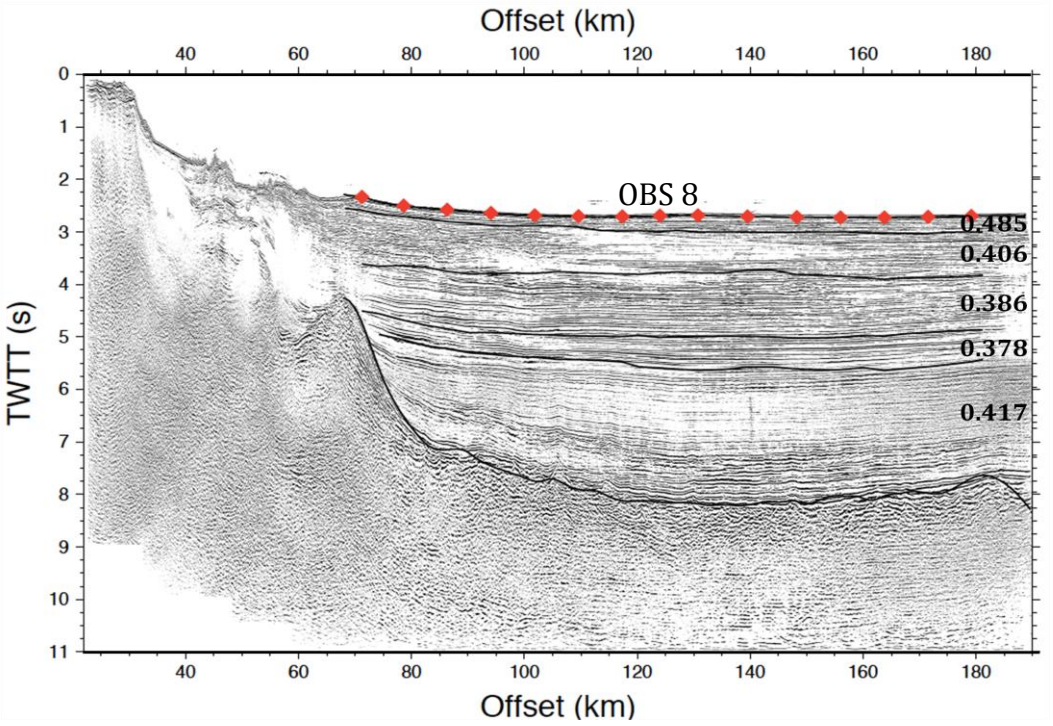

Figure 3.6: Modeled reflections plotted over coincident MCS data provided by TPAO. σ values are written at the right of the figure. The red diamonds represent the positions of the OBS and the black lines the modelled reflectors.

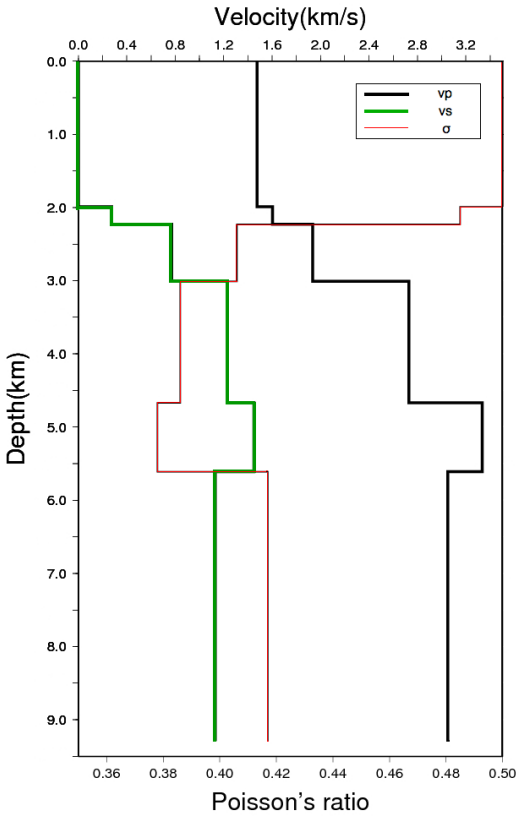

Figure 3.7: Best-fitting P- and S-wave velocities and Poisson's ratio at OBS 8 vs. depth. The black thick line represents the P-wave velocity, the green line the S-wave velocity and the red line represents σ.

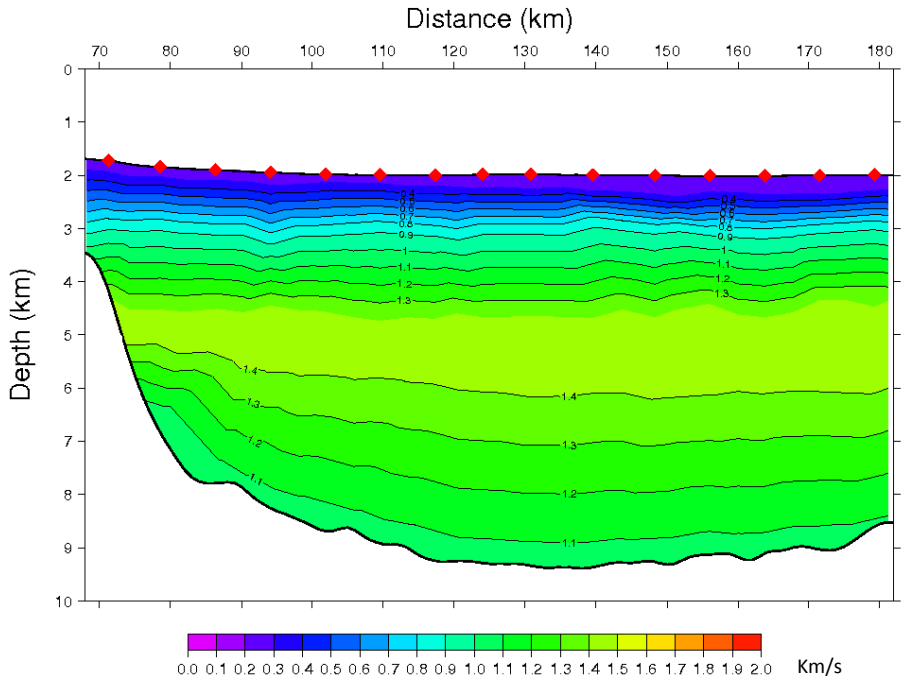

Figure 3.8: S wave velocity-depth model of Line 2. The red diamonds are the OBS, the black line is R.5, the reflection that represents the acoustic basement.

Chapter 4: Uncertainties of the model parameters

Our model includes three parameters, P-wave velocity, layer thickness and σ. To estimate the error of each parameter I kept one parameter fixed and perturbed the other two until the rms traveltime residuals exceeded the pick uncertainty. In Table 2 I present the resulting estimates.

Layer	Error Poisson's Ratio σ	Error v_p (km/s)	Error v_s (km/s)	Layer Thickness (km)
1	±0.002	±0.15	±0.11	±0.01
2	±0.013	±0.19	±0.13	±0.01
3	±0.021	±0.31	±0.22	±0.01
4	±0.032	±0.56	±0.39	±0.02
5	±0.022	±0.45	±0.31	±0.03

Table 2: The first column indicates the number of each layer and the following four columns show the σ, P-wave velocity, S-wave velocity and layer thickness errors, respectively, of those layers.

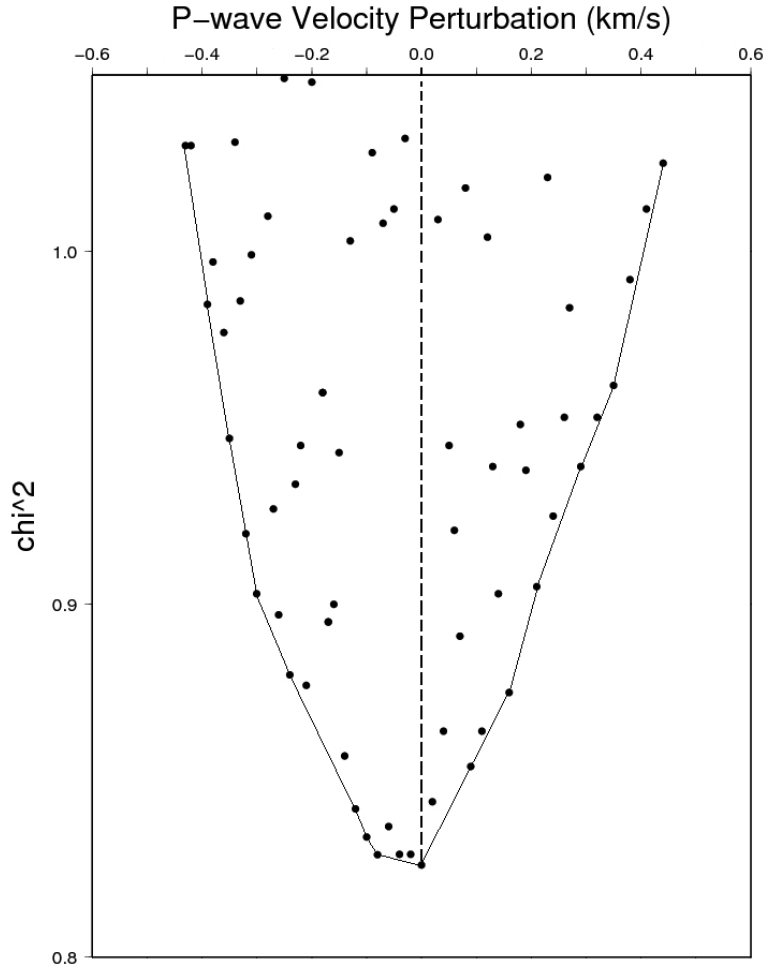

Figure 4.1: All the acceptable values of P-wave velocity, for the fifth layer, are plotted against χ^2. We can see that the value with the smallest χ^2 value is the one in our final model. The depth has also been perturbed and the line marks the lowest χ^2 for each value of P-wave velocity.

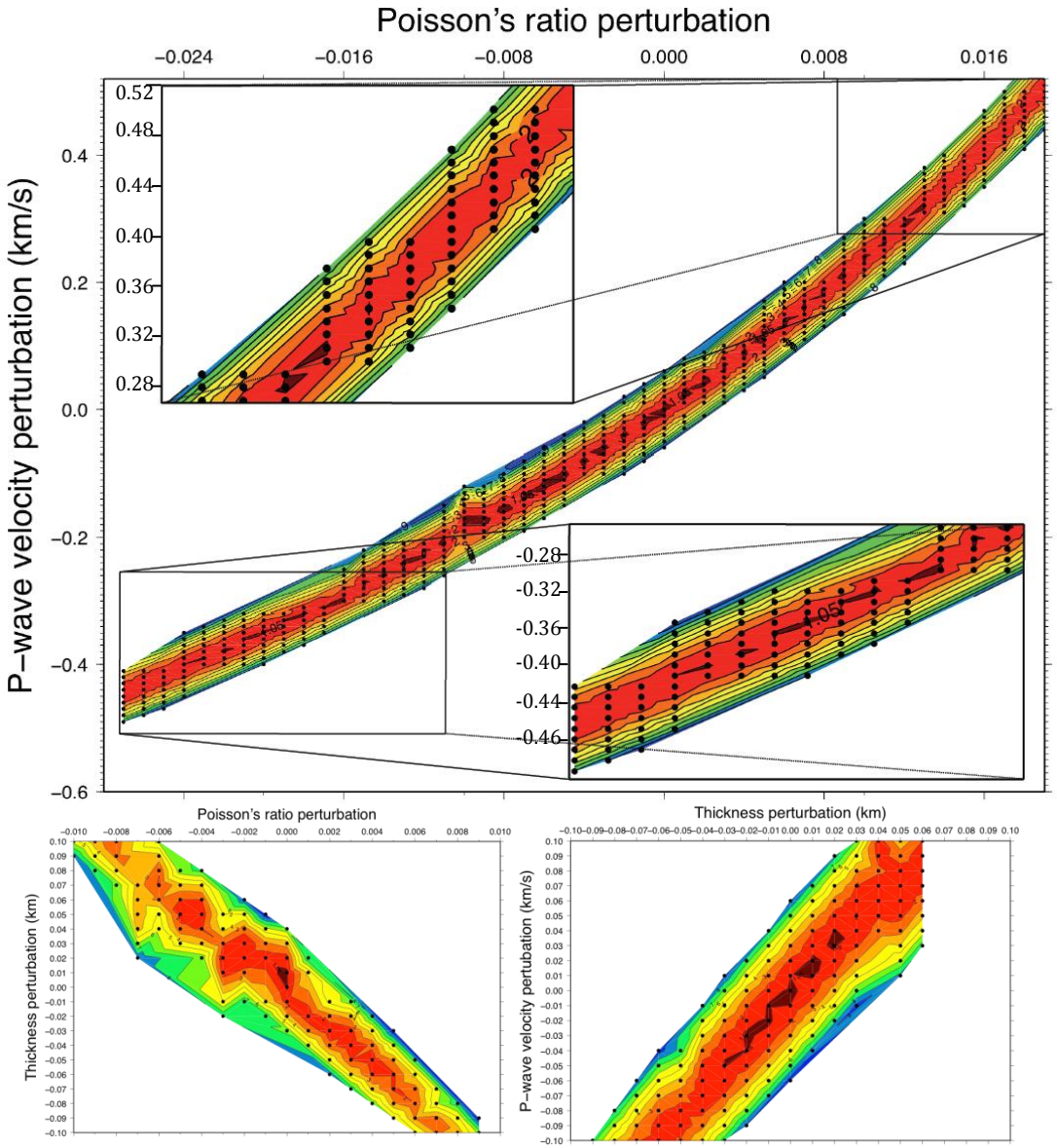

Figure 4.2: Contours of χ^2 as a function of two parameters as the third is kept fixed. In the top panel the thickness of the layer is kept fixed. In the bottom left panel the P-wave velocity is kept fixed and in the bottom right panel Poisson's ratio is kept fixed. The dark red regions are considered acceptable fits (χ^2<1.05).

Chapter 5: Rock physics modelling

Using the values of V_p, V_s and σ derived from forward modelling I estimate porosities, densities and aspect ratios using DEM theory. To estimate the matrix values I used the Voigt-Reuss-Hill average (equations 8).

$$K_s = \frac{1}{2}[(1-C)K_q + CK_c + \frac{1}{(1-C)/K_q + C/K_c}]$$
$$\mu_s = \frac{1}{2}[(1-C)\mu_q + C\mu_c + \frac{1}{(1-C)/\mu_q + C/\mu_c}]$$
$$\rho_s=(1-C)\ \rho_q + C\rho_c \quad (8)$$

The equations here are given for a quartz/clay mixture. K_s and μ_s are bulk and shear moduli of all the constituents of the solid phase, respectively; ρ_s is the density of the solid phase; C is the volume fraction of clay content in the solid phase; the subscripts "q" and "c" refer to quartz and clay, respectively. To estimate the clay content of the solid phase I used the velocity gradients of the top 2-3 km of sediments. The velocity of P-waves steadily increases with depth, with a vertical gradient of ~0.7 s^{-1}(Scott *et al.*, 2009). For a shale lithology one would expect a velocity gradient in the upper sediments of ~0.55 s^{-1}, while for a sand lithology the gradient would be ~1-1.15 s^{-1} (Japsen *et al.*, 2007). The above velocity gradients suggest that I should use a matrix composition of 60% shale and 40% sand. In Shillington et al. (2008) there is a suggested lithology of the centre of Eastern Black Sea basin estimated from onshore geological mapping, existing well controlled and seismic reflection data that suggests a matrix composition of ~85% shale and 15% sand but since it is not exactly on the location of Line 2 I chose to work with the composition that was suggested by the velocity gradients. The starting medium is of zero porosity and I then add brine inclusions using DEM. The values of the moduli of each constituent are presented in Table 3.

Component	Bulk Mod. (GPa)	Shear Mod. (GPa)	Density (g/cm^3)
Clay	21	7	2.6
Quartz	36.6	45	2.65
Brine	2.29	0	1.025

Table 3: The first column shows the components used in the calculations. The first two were used as matrix components and brine as inclusions. The other three columns show the Bulk and Shear modulus and the density of each component respectively taken by Mavko et.al, (1998).

The original P-wave velocity model had values every 250 m in depth and every 1 km in distance. I have assigned to each velocity value a porosity, density and aspect ratio value from DEM modeling as presented in table 3.

In order to quantify how good the model is, I used least squares to estimate the residuals between V_s and V_p values calculated by forward modeling (V_{pobs}, V_{sobs}) and the V_s and V_p values calculated by DEM theory (V_{pcalc}, V_{scalc}). The formula that I used is:

$$rms = \sqrt{\lambda_1 \frac{(V_{pcalc} - V_{pobs})^2}{V_{pobs}^2} + \lambda_2 \frac{(V_{scalc} - V_{sobs})^2}{V_{sobs}^2}} \qquad (9)$$

where

$$\frac{\lambda_2}{\lambda_1} = \left[\frac{Error(V_{pobs})\%}{Error(V_{sobs})\%}\right]^2 \qquad (10)$$

Figure 5.1 shows contour plots of the rms of the second point of the first layer along with lines of equal porosity and equal aspect ratio. The green dot has the values of σ and V_p, V_s at 250 meters depth at OBS 8. The black dots are produced by DEM model and are considered them to be model points with specific values of σ, V_p, V_s, aspect ratio and porosity. The best modelled layer has porosity of 58%, aspect ratio of the brine inclusions of 0.05, giving residuals between the calculated velocities by forward modeling and the velocities calculated by DEM of rms=1,70 10^{-5}. In table 3 I present

the aspect ratios, porosities and densities of all the layers of OBS 5. Figure 5.2 shows the variation of porosity in line 2 and Figures 5.3 and 5.4 the variation of density and aspect ratio, respectively.

Depth (km)	**Aspect ratio α**	**Porosity φ %**	**Density (g/cm^3)**
0	0.04	55	1.7427
0.25	0.06	43	1.9342
0.5	0.02	36	2.0458
0.75	0.035	28	2.1734
1	0.035	24	2.2372
1.25	0.025	17	2.3488
1.5	0.02	12	2.4286
1.75	0.0085	5	2.5402
2	0.007	4	2.5562
2.25	0.0055	3	2.5721
2.5	0.006	3	2.5721
2.75	0.004	2	2.5881
3	0.045	2	2.5881
3.25	0.0045	2	2.5881
3.5	0.0045	2	2.5881
3.75	0.003	2	2.5881
4	0.003	2	2.5881
4.25	0.003	2	2.5881
4.5	0.0045	3	2.5721
4.75	0.004	3	2.5721
5	0.0055	4	2.5562
5.25	0.0065	5	2.5402
5.5	0.008	6	2.5243
5.75	0.0075	6	2.5243
6	0.009	7	2.5084
6.25	0.0085	7	2.5084
6.5	0.01	8	2.4924
6.75	0.01	8	2.4924
7	0.01	8	2.4924
7.25	0.0085	7	2.5084

Table 4: In the first column there is the depth below sea bed to which each value corresponds. The second column has the aspect ratio of the brine inclusions and the third layer the porosity that was the best fit. The fourth column shows the density. The values correspond to 148th km on the line or to the 5th OBS.

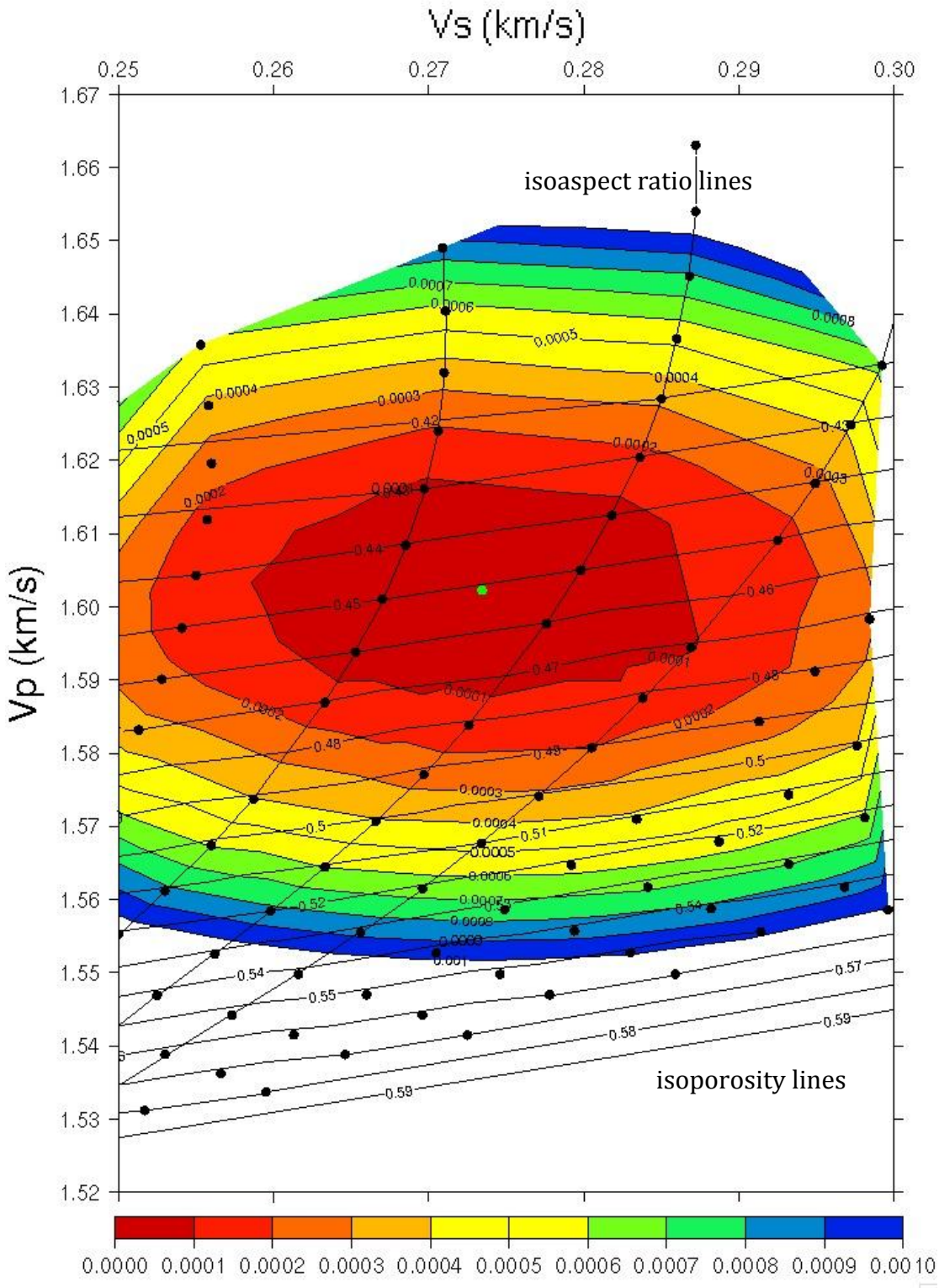

Figure 5.1: Contour plot of the residuals between the velocity values of OBS 8 calculated by forward modelling and by DEM at 250 meters depth. The green dot represents the second point of our forward model, at 250 meters depth below seabed, having the model's velocities and σ. Each black dot corresponds to values of velocities, density and aspect ratio calculated by DEM theory. The lateral lines indicate the porosity of those layers and the vertical lines the aspect ratio of the inclusions in that layer. The uncertainties of the velocities for this layer are ± 0.15 km/s for the P-wave and ± 0.11 km/s for the S-wave velocity. We can see that many models calculated from DEM fit the layer within its uncertainties but we pick the one with the smallest RMS.

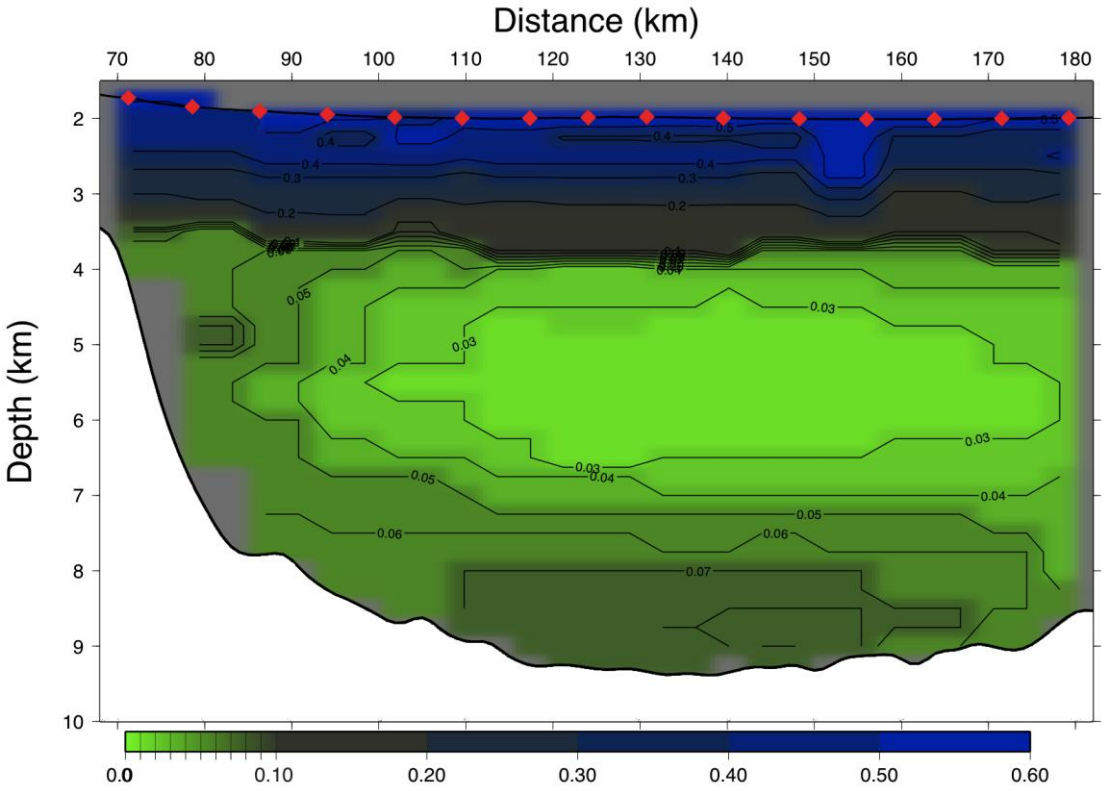

Figure 5.2: Porosity values in Line 2.Within the low velocity zone the porosity increases instead of decreasing with depth. The red diamonds represent the OBS and the thick black lines the seabed and acoustic basement. Porosity is a dimensionless quantity.

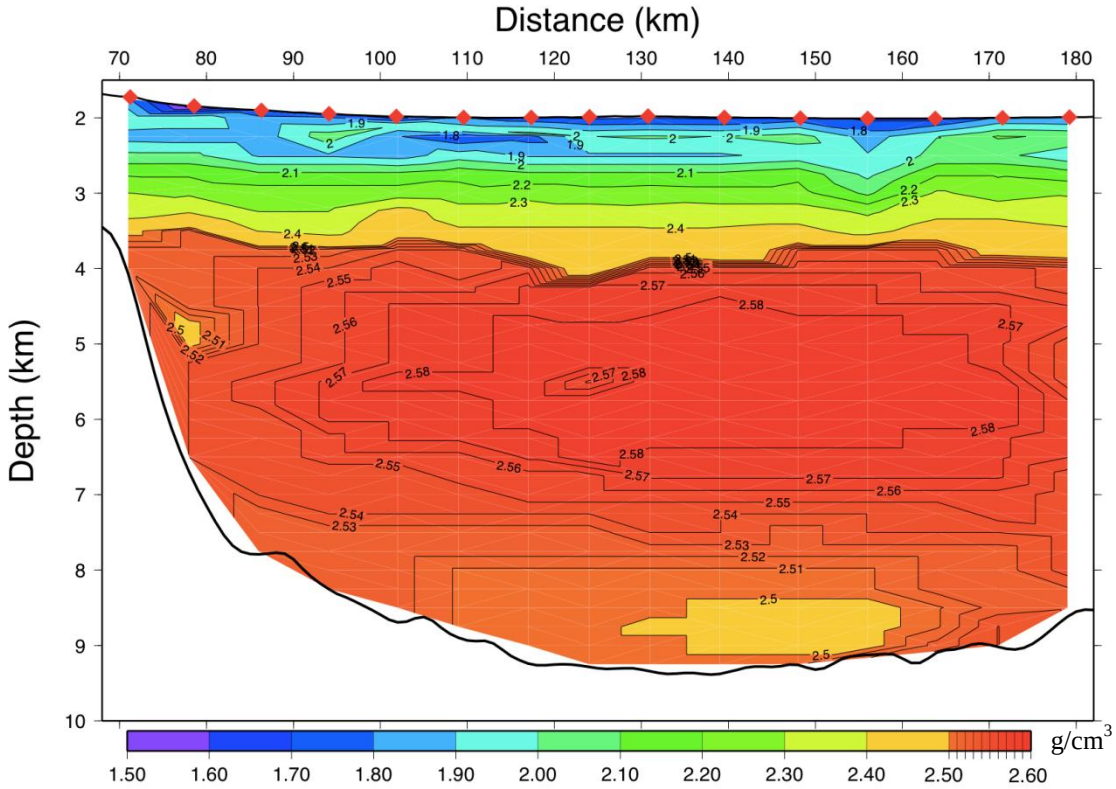

Figure 5.3: Density change in Line 2. With increasing load the density of the sediments should increase with depth. In the low velocity zone the density decreases with depth.

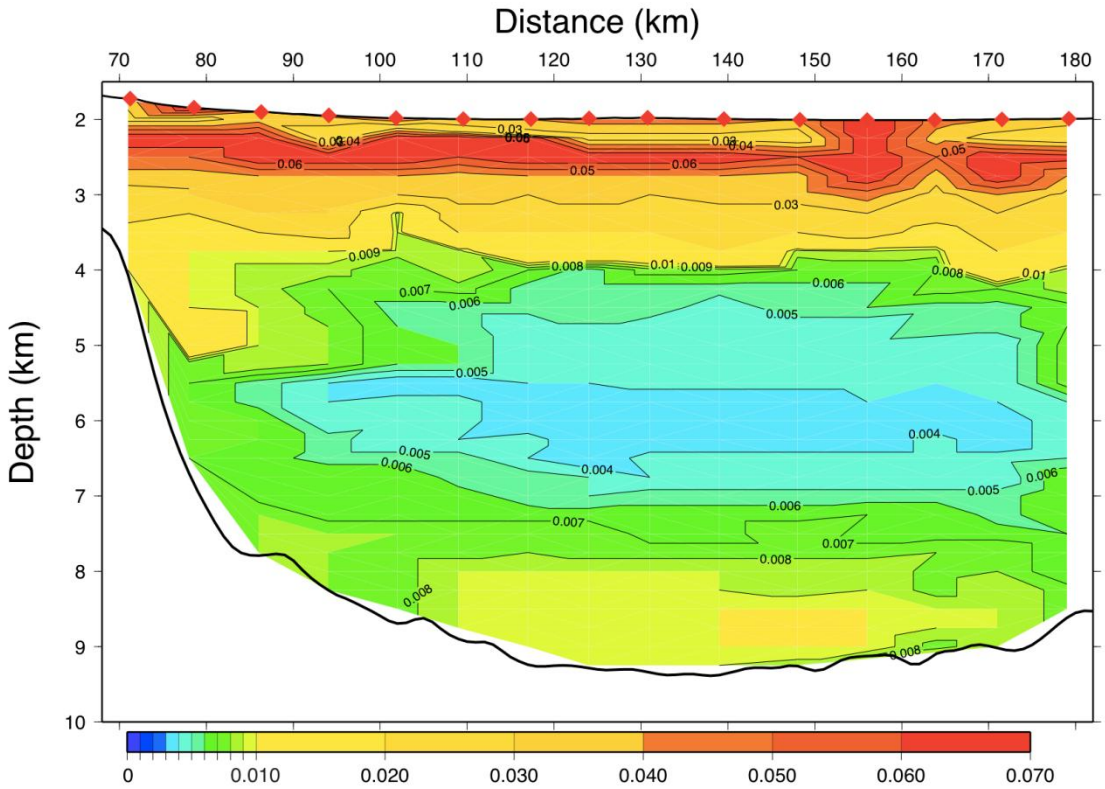

Figure 5.4: Aspect ratio change in Line 2.Much like the previous figures aspect ratio begins to increase in the low velocity zone, while it is expected to decrease. Aspect ratio is a dimensionless quantity.

Chapter 6: Pore pressure estimation

6.1 Calibration of Athy's law

In the Eaton method, as described above, it is easy to understand that the key point to its implementation is the calculation of V_{norm}. To do that one is required to make assumptions about the structure of sediments with a normal compaction history and hydrostatic pore pressures since there are no borehole data for the deeper layers in the Black Sea. My assumption is to take an Athy compaction curve for porosity (Athy, 1930) as the porosity structure for normal pressurised sediments and calibrate it using my porosity structure for the first 3 kilometres of sediments. The Athy formula for porosity is:

$$\varphi=\varphi_0 e^{\alpha z} \qquad (11)$$

where φ_0 is the surface porosity and α is the compaction factor which we will calibrate using my porosities.

In Figure 6.1 we see our porosity structure of OBS 11 and porosity structures for different values of α.

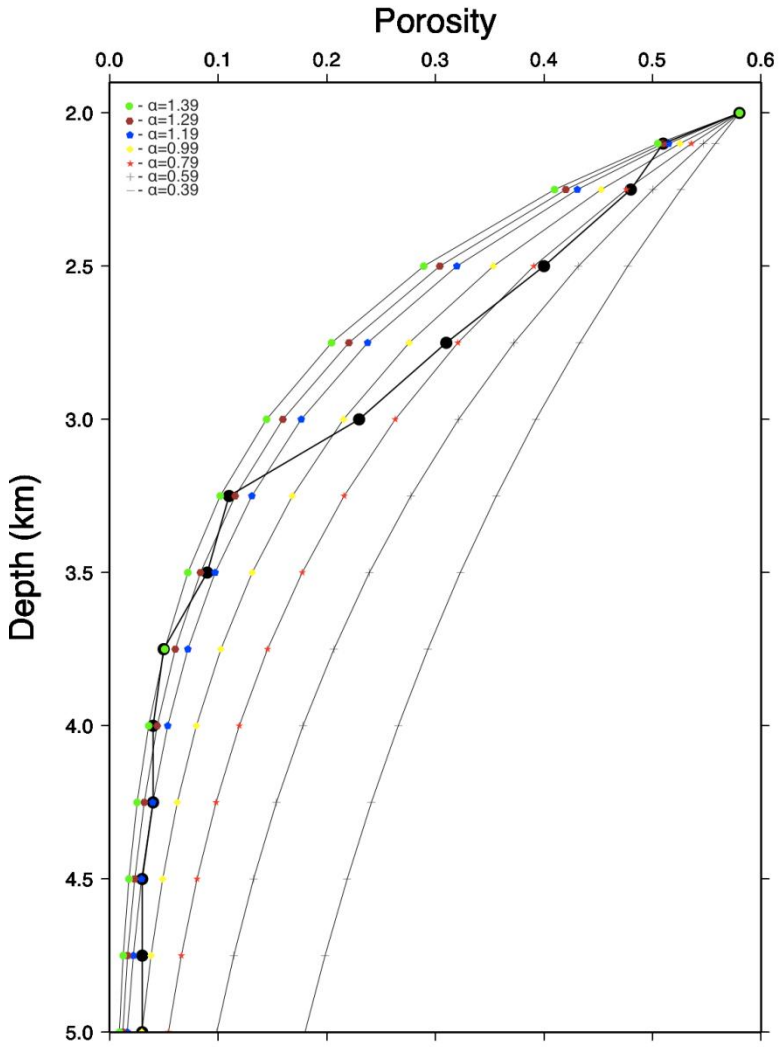

Figure 6.1: The thick black line and the black circles represent the porosity structure of OBS 11. Each other symbol represents a different value of α

In order to understand better which value of α produces the best fit I use equation 12 to estimate the residuals of every α value.

$$rms = \sqrt{\sum_{i=1}^{14}(\varphi_{calc} - \varphi_{bor})_i^2} \qquad (12)$$

where i shows the depth that each value of porosity corresponds to.The value with the lowest residuals is the chosen one. In Figure 6.2 we see that this value is α =1.18.

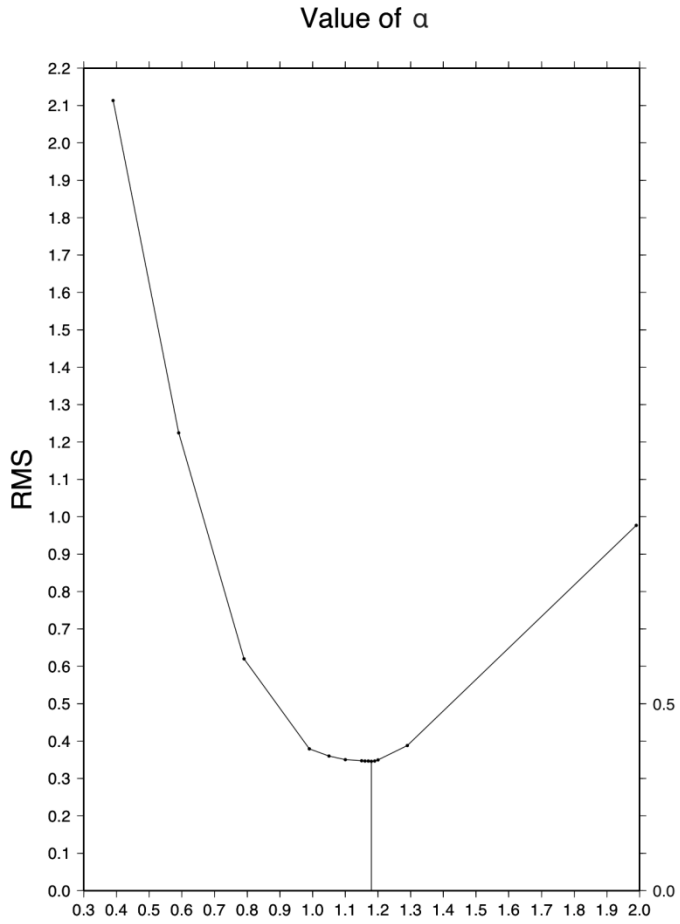

Figure 6.2: The values presented in this graph are:
α =0.39, 0.59, 0.79, 0.99, 1.05, 1.10, 1.15, 1.16, 1.17, 1.18, 1.19, 1.20, 1.29, 1.99 and the one with the minimum residuals is 1.18.

After having calculated the porosity structure for the normal pressurized sediments I calculate the V_{norm} using the Raymer equation (Mavko *et al.*, 2003) for shale lithology which is as follows:

$$V_{norm}=(1-\varphi)^2V_0+\varphi V_f \quad (13)$$

where V_0 is the mineral velocity set to 4.750 km/s (average sale velocity (Schon, 1996)) and V_f is the fluid velocity set to 1.465 km/s (EBS sea-water velocity).

6.2. Calibration of the Eaton method

The calibration of the Eaton method (eq.4) relies on the calibration of the exponent n. Unfortunately the only suitable borehole data in the area are in the western part of the EBS, far away from line 2. Since they are the only borehole measurements that we have we use them to calibrate the exponent n (Figure 6.3).

In order to be certain which value of n gives the best fit we used equation 14 to estimate the rms of each n value, where i corresponds to the pore pressure values at a certain depth. The value of n that corresponds to the lowest sum is the optimal fit (Figure 6.4).

$$rms = \sqrt{\sum_{i=1}^{6}(P_{calc} - P_{bor})_i^2} \quad (14)$$

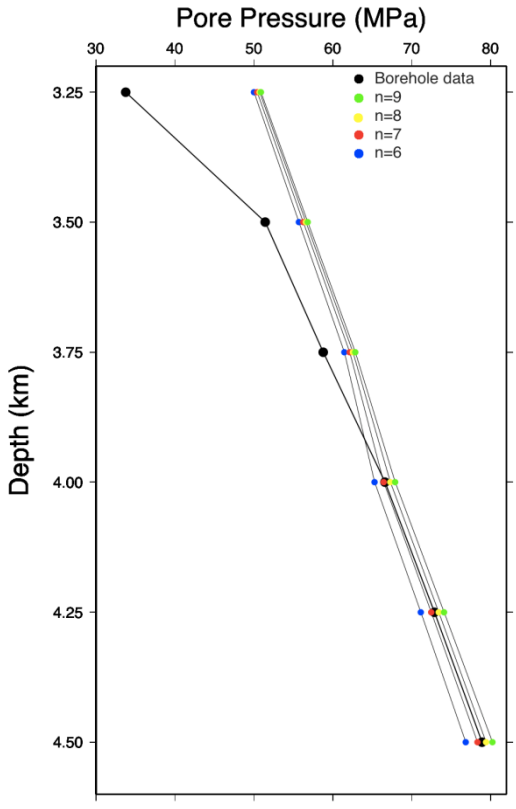

Figure 6.3: Calibration of the exponent n. The black dots represent the borehole data and the colored ones pore pressures calculated with Eaton method with different n.

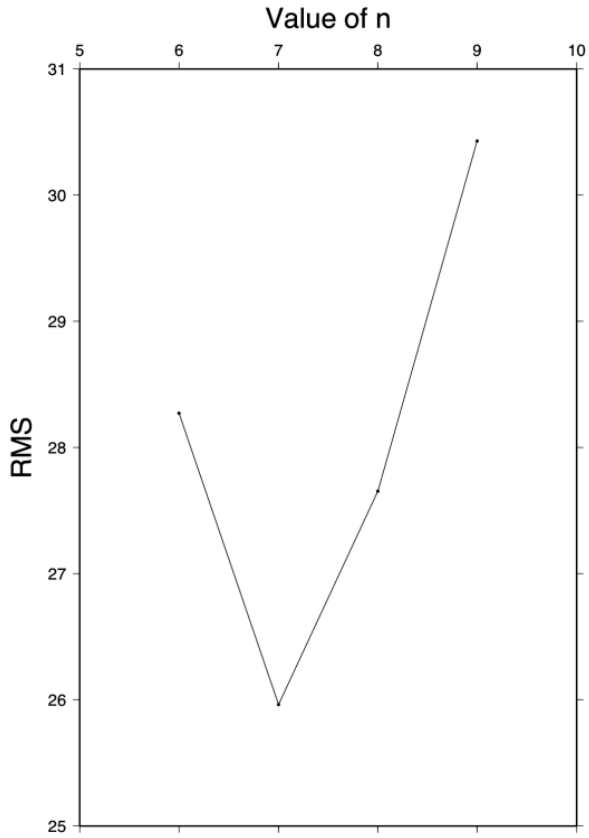

Figure 6.4: The rms of the previous values of n show clearly that the best fit is provided by n=7.

Having calibrated the exponent of equation 4 we calculate pore pressures for line 2 (Figure 6.5).

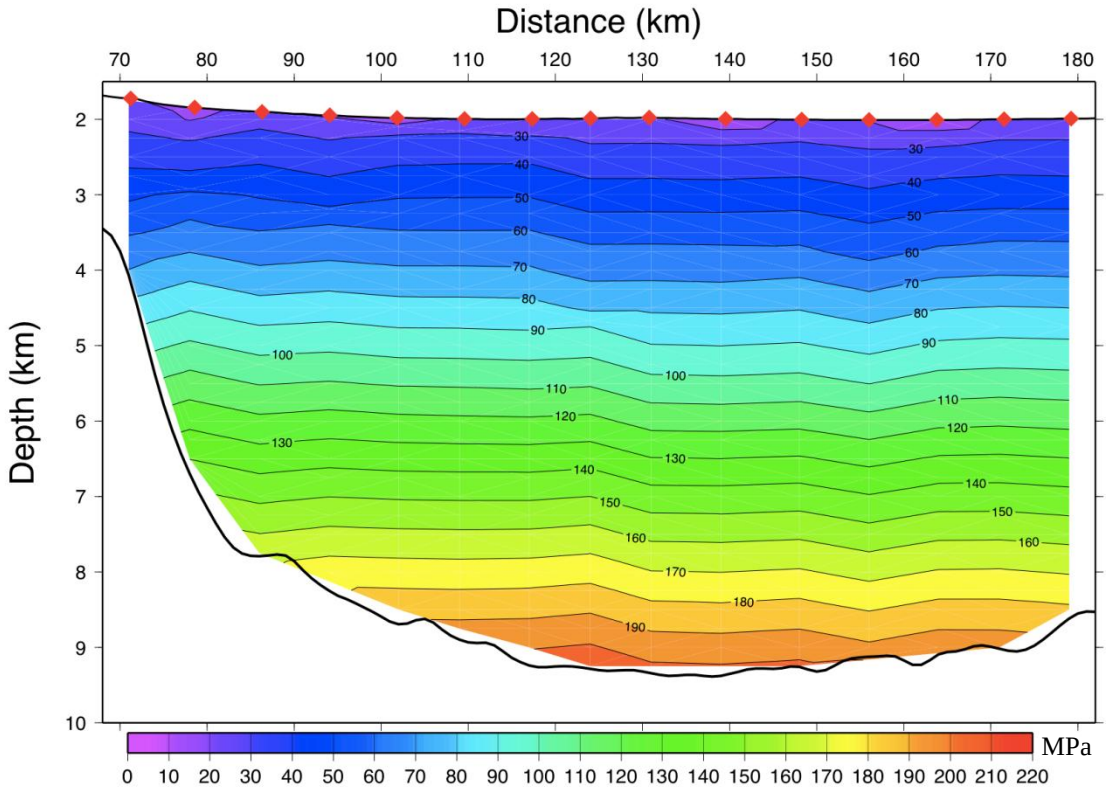

Figure 6.5: Change of pore pressure in Line 2.

To evaluate the degree of overpressure in comparison to the hydrostatic effective stress (the difference between confining stress and hydrostatic pore pressure) in deep water environment, we used the normalized pore pressure ratio λ* (Screaton *et al.*, 2002) defined as :

$$\lambda^* = \frac{P_f - P_{hf}}{L_p - H_p} \tag{15}$$

Our results give λ* values around 0.9 across the greatest part of line 2 (Figure 6.6). A value of $\lambda^* \geq 1$ would mean that the pore pressure is great enough to fracture the overburden, allowing pore contents to escape to the surface. Although the Eaton method cannot produce results that would give $\lambda^* \geq 1$ there is no sign of fracturing of the overburden in Line 2 and this supports our calculation that λ* values are high but do not reach 1.

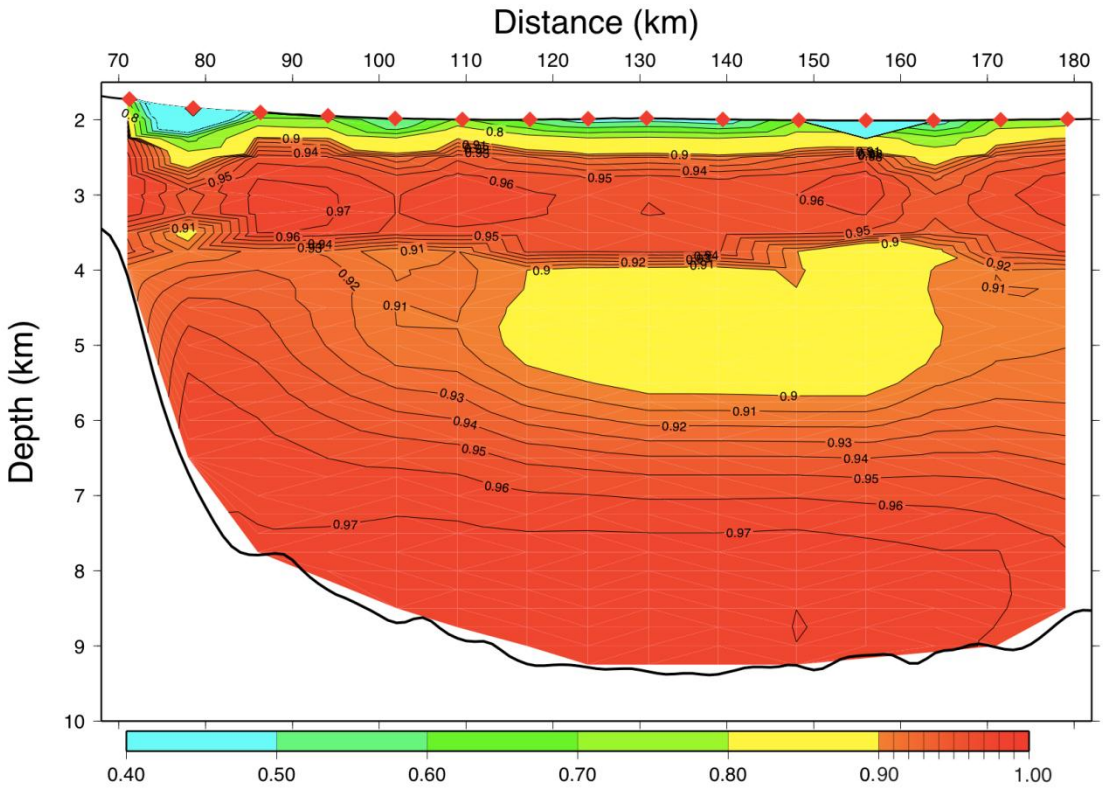

Figure 6.6: λ* variation in Line 2. From the 3rd until approximately the 5th km there is a decrease of λ* which means that above the low velocity zone the overpressure decreases. In the low velocity zone λ* values increase again and reach the value of 0.97. λ* is a dimensionless quantity.

Chapter 7: Discussion

I have presented a P-S converted wave velocity model based on the P-wave velocity depth model of Scott et al. (2009). The S-wave model includes five layers; three more than the starting P-wave model. To achieve this I had to examine as many models for each reflection as possible to see which has the best fit (the lowest residuals). The transforming boundaries were found across the entire Line 2 and were visible from all OBS used, although in some the reflection was stronger than in others. The picking uncertainty that I had assigned 15 ms, which is considered to be a low value but the data fulfilled this condition. The errors for each parameter of the model were calculated using Katzman's et al. (1994) method and were shown to be quite low. I used DEM theory to calculate the physical properties of the sediments and estimated pore pressures by using the Eaton method which I calibrated with these values and borehole data. The physical properties that were given from DEM were constrained by both P and S- wave velocities. DEM gave results regarding the aspect ratio, porosity and density across the Line.

One of the most interesting result produced is the variation of aspect ratio with depth. Aspect ratio of the water inclusions inside the sediments is expected to reduce with depth due to the gravitational force that becomes bigger. This is the case in the study area until approximately 4 km below sea bottom where aspect ratio begins to increase. At this depth is the beginning of the low velocity zone. The interesting part is that, according to theories why overpressures occur (Osborne and Swarbrick, 1997), if there is a depth beyond which fluids start to be retained by the sediments, something that would lead to increase in aspect ratio of the inclusions, then the over pressures are due to increase of compressive stress. This result is in agreement with

other works from the same study area (Marin-Moreno et al., 2013a; Marin-Moreno et al., 2013b).

The pore pressure results that I have estimated are quite similar to those of Scott al. (2009). In a way this was something expected due to the fact that we both used the same borehole data to calibrate the model. The lack of boreholes close to my study area was a great limitation for this study. The one that helped me calibrate the data in not on Line 2 and it gave pressures for 1.25 km, from 3.25km to 4.50km below sea level. Because of this limitation I had to take under consideration for the lithology components of the matrix the P-wave velocity vertical gradient given in Scott et al (2009), although my model was much more detailed. The calibration of Athy's law gave a value of the compactions factor α=1.18. Scott et al. (2009) estimated a compaction factor of α=0.48 or 0.58 for the easternmost part of the basin. The main difference in these results is that ours were calibrated by the porositites produced by DEM while Scott et al. (2009) calibrated it using P-wave velocities. Calibration of Eaton method gave an n value of 7 while Scott et al., (2009) used a value of 8 so the difference is not that great.

Another difference between the method presented here and that of Scott et al. (2009) work is in the λ^* estimation. Scott et al. (2009) used a single density value for the entire line (ρ_m=2700 kg/m^3 which is an average shale value (Schon, 1996)) a value greater than all of the values that DEM produced for the given matrix composition. This difference led, in our case, to smaller values of lithostatic pressure and given the similarity of the pore pressure results, to greater λ^* values (Equation 15). This means that in our study Line 2 in much more overpressured than in Scott et al., (2009) who gave values of λ^* close to 0.4 ~5km below sea level and 0.9 ~9km below sea level while in our study λ^* values increase to 0.9 from ~2.5 km below sea level. This high

value of λ* could be because of the fact that pore pressures are affected by processes other than disequilibrium compaction, e.g. the current compressional tectonics affecting the margins of the EBSB. In a sedimentary basin, it is normally assumed that the vertical effective stress is the maximum principal effective stress and the minimum effective stress is horizontal (e.g. Daigle & Dugan, 2010). In this context, the ratio of horizontal to vertical effective stress K_0 is usually 0.6 (Karig & Hou, 1992). Hydraulic fracturing will occur with pore pressures greater than the minimum horizontal effective stress, and so with values of $\lambda^* > 0.6$. However, in our case, we can neither assume that the minimum principal effective stress is horizontal or that K_0 is equal to 0.6 due to the compressional tectonics affecting the margins of the EBSB. The presence of mud volcanoes near the east coast of the EBSB (Kruglyakova et al., 2004), where essentially is Line 2, indicates the presence of hydraulic fracturing and so pore pressures greater than the minimum principal effective stress.

Chapter 8: Conclusions

1. The Eastern Black Sea Basin sediments have a maximum thickness of ~ 9.2 km along our survey line.
2. S-wave velocity varies from ~0.22 km/s at the seabed to ~1.55 km/s at ~4.5km depth.
3. A widespread low velocity zone spans from 5.5 km depth to the top of the acoustic basement, indicated by a velocity decrease from ~3.30 to ~2.80 km/s for the P-wave velocity and from ~1.5 to ~1.1 km/s for the S-wave velocity.
4. Poisson's ratio varies from 0.485 at the seabed to 0.378 in the 4^{th} layer (approximately from 4.5 to 5.5 km below sea level).
5. Poisson's ratio increases inside the low velocity zone, which means that the S-wave velocity decreases along with the P-wave velocity.
6. Porosity decreases from ~58% at the top of the first layer to ~1% at the bottom of the 4^{th} and at the top of the last layer. In the low velocity zone porosity increases to ~7% at the bottom
7. Aspect ratio decreases with depth until the low velocity zone from ~0.070 to ~0.004 and then increases again to ~0.008 at the acoustic basement.
8. The density of the sediments varies from ~1.8 g/cm^3 at the sea floor to ~2.58 g/cm^3 at the top of the low velocity zone. In the low velocity zone there is a decrease of density to ~2.5 g/cm^3 at the top of the acoustic basement.
9. Pore pressure varies from ~20MPa at sea floor to ~200MPa at the top of Cretaceous, at average depth 8.5km below sea level..
10. The values of λ^* vary from ~0.4 at the sea floor to ~0.97 at the bottom of the sediments.

Bibliography

Athy, L.F., 1930. Density,porosity and compaction of sedimentary rocks., *AAPG Bulletin,* 14**,** 1-24.

Audet, D. M., & McConnell, J. D. C. (1992). Forward modelling of porosity and pore pressure evolution in sedimentary basins. *Basin Research*, *4*(2), 147-162.

Avellaneda, M., 1987. Iterated Homogenization, Differential Effective Medium Theory and Applications, *Commun Pur Appl Math,* 40**,** 527-554.

Bakan, G. & Buyukgungor, H., 2000. The Black Sea, *Marine Pollution Bulletin,* 41**,** 24-43.

Banks, C.J. & Robinson, A., 1997. Mesozoic strike-slip back-arc basins of the western Black Sea region. In:Robinson, A.G. (Ed.), Regional and petroleum geology of the Black Sea and surrounding region, *AAPG Memoir,* 68**,** 53-61.

Banks, C. J. (1998). Basins and thrust belts of the Balkan Coast of the Black Sea. *MEMOIRS-AMERICAN ASSOCIATION OF PETROLEUM GEOLOGISTS*, 115-128.

Berge, P.A., Berryman, J.G. & Bonner, B.P., 1993. Influence of Microstructure on Rock Elastic Properties, *Geophysical Research Letters,* 20**,** 2619-2622.

Berryman, J.G., 1992. Single-Scattering Approximations for Coefficients in Biot Equations of Poroelasticity, *Journal of the Acoustical Society of America,* 91**,** 551-571.

Berryman, J.G. & Berge, P.A., 1993. Rock elastic properties;Dependence on microstructure,in Homogenization and constitutive modeling for heterogeneous material, *ASME AMD,* 166**,** 1-13.

Berryman, J.G., Berge, P.A. & Bonner, B.P., 2002. Estimating rock porosity and fluid saturation using only seismic velocities, *Geophysics,* 67**,** 391-404.

Bredehoeft, J. D., Djevanshir, R. D., & Belitz, K. R. (1988). Lateral fluid flow in a compacting sand-shale sequence: South Caspian Basin. *AAPG Bulletin*, *72*(4), 416-424.

Bruggeman, D.A.G., 1935. Berechnung vershiedener physikalisher kostanten von heterogenen substanzeb I. Dielecktrizitatskonstaten und leitfahigkeiten der mischkorper aus isotropen substanzen, *Ann. Physik (Leipzig),* 24**,** 636-679.

Bünz, S., Mienert, J., Vanneste, M., & Andreassen, K. (2005). Gas hydrates at the Storegga Slide: Constraints from an analysis of multicomponent, wide-angle seismic data. *Geophysics*, *70*(5), B19-B34.

Burg, J. P., Ricou, L. E., Klain, L., Ivanov, Z., & Dimov, D. (1996). Crustal-scale thrust complex in the Rhodope massif. In *The Tethys Ocean* (pp. 125-149). Springer US.

Burst, J. F. (1969). Diagenesis of Gulf Coast clayey sediments and its possible relation to petroleum migration. *AAPG bulletin*, *53*(1), 73-93.

Carcione, J.M. & Helle, H.B., 2002. Rock physics of geopressure and prediction of abnormal pore fluid pressures using seismic data.

Carcione, J. M., Helbig, K., & Helle, H. B. (2003). Effects of pressure and saturating fluid on wave velocity and attenuation in anisotropic rocks.*International Journal of Rock Mechanics and Mining Sciences*, *40*(3), 389-403.

Carcione, J. M., Helle, H. B., Pham, N. H., & Toverud, T. (2003). Pore pressure estimation in reservoir rocks from seismic reflection data. *Geophysics*, *68*(5), 1569-1579.

Daigle, H., & Dugan, B. (2010). Origin and evolution of fracture-hosted methane hydrate deposits. *Journal of Geophysical Research: Solid Earth (1978–2012)*,*115*(B11).

Dickinson, G. (1953). Geological aspects of abnormal reservoir pressures in Gulf Coast Louisiana. *AAPG Bulletin*, *37*(2), 410-432.

den Boer, L.D., Sayers, C. M., Nagy, Z., Hooyman, P., Woodward, M. J., 2006. Pore pressure prediction using well-conditioned seismic velocities, *First Break,* 24.

Dutta, N.C., 2002. Geopressure prediction using seismic data: Current status and the road ahead, *Geophysics,* 67**,** 2012.

Dvorkin, J. & Nur, A., 1996. Elasticity of high-porosity sandstones: Theory for two North Sea data sets, *Geophysics,* 61**,** 1363-1370.

Eaton, B. A. (1972). The effect of overburden stress on geopressure prediction from well logs. *Journal of Petroleum Technology*, *24*(08), 929-934.

Eaton, B.A., 1976. Graphical Method Predicts Geopressures Worldwide, *World Oil,* 183**,** 100-104.

Eberhart-Phillips, D., 1989. Empirical relationships among seismic velocity, effective pressure, porosity, and clay content in sandstone, *Geophysics,* 54**,** 82.

Ershov, A. V., Brunet, M. F., Korotaev, M. V., Nikishin, A. M., & N Bolotov, S. (1999). Late Cenozoic burial history and dynamics of the Northern Caucasus molasse basin: implications for foreland basin modelling. *Tectonophysics*,*313*(1), 219-241.

Ershov, A. V., Brunet, M. F., Nikishin, A. M., Bolotov, S. N., Nazarevich, B. P., & Korotaev, M. V. (2003). Northern Caucasus basin: thermal history and synthesis of subsidence models. *Sedimentary Geology*, *156*(1), 95-118.

Freed, R. L., & Peacor, D. R. (1989). Geopressured shale and sealing effect of smectite to illite transition. *AAPG Bulletin*, *73*(10), 1223-1232.

Golmshtok, A.Y., Zonenshain, L.P., Terekhov, A.A. & Shainurov, R.V., 1992. Age, Thermal Evolution and History of the Black-Sea Basin Based on Heat-Flow and Multichannel Reflection Data, *Tectonophysics,* 210**,** 273-293.

Gorur, N., 1988. Timing of Opening of the Black-Sea Basin, *Tectonophysics,* 147**,** 247-262.

Granli, J.R., Arntsen, B., Sollid, A. & Hilde, E., 1999. Imaging through gas-filled sediments using marine shear-wave data, *Geophysics,* 64**,** 668-677.

Haacke, R.R. & Westbrook, G.K., 2006. A fast, robust method for detecting and characterizing azimuthal anisotropy with marine PS converted waves, and its application to the west Svalbard continental slope, *Geophysical Journal International,* 167**,** 1402-1412.

Han, D.-H., 1986. Effects of porosity and clay content on wave velocities in sandstones, *Geophysics,* 51**,** 2093.

Han, D. H., Nur, A., & Morgan, D. (1986). Effects of porosity and clay content on wave velocities in sandstones. *Geophysics*, *51*(11), 2093-2107.

Hubbert, M.K. & Rubey, W., 1959. Role of fluid pressure in mechanics of overthrust faulting, Pts. I and II, *Geological Society of America Bulletin,* 70**,** 115-205.

Hyndman, R.D. & Spence, G.D., 1992. A seismic study of methane hydrate marine bottom simulating reflectors, *Journal of Geophysical Research,* 97**,** 6683-6698.

Japsen, P., Mukerji, T. & Mavko, G., 2007. Constraints on velocity-depth trends from rock physics models, *Geophysical Prospecting,* 55**,** 135-154.

Karig, D. E., & Hou, G. (1992). High-stress consolidation experiments and their geologic implications. *Journal of Geophysical Research: Solid Earth (1978–2012)*, *97*(B1), 289-300.

Kruglyakova, R. P., Byakov, Y. A., Kruglyakova, M. V., Chalenko, L. A., & Shevtsova, N. T. (2004). Natural oil and gas seeps on the Black Sea floor. *Geo-Marine Letters*, *24*(3), 150-162.

Kuster, G.T. & Toksoz, M.N., 1974. Velocity and Attenuation of Seismic-Waves in 2-Phase Media .1. Theoretical Formulations, *Geophysics,* 39**,** 587-606.

Li, X.-Y., Dai, H., Mueller, M.C. & Barkved, O.I., 2001. Compensating for the effects of gas clouds on C-wave imaging: A case study from Valhall, *The Leading Edge,* 20**,** 1022-1028.

Mann, D. M., & Mackenzie, A. S. (1990). Prediction of pore fluid pressures in sedimentary basins. *Marine and Petroleum Geology*, *7*(1), 55-65.

Marín-Moreno, H., Minshull, T. A., & Edwards, R. A. (2013). Inverse modelling and seismic data constraints on overpressure generation by disequilibrium compaction and aquathermal pressuring: application to the Eastern Black Sea Basin. *Geophysical Journal International*, *194*(2), 814-833.

Marín-Moreno, H., Minshull, T. A., & Edwards, R. A. (2013). A disequilibrium compaction model constrained by seismic data and application to overpressure generation in The Eastern Black Sea Basin. *Basin Research*, *25*(3), 331-347.

Marine, I. W., & Fritz, S. J. (1981). Osmotic model to explain anomalous hydraulic heads. *Water Resources Research*, *17*(1), 73-82.

Mavko, G., Mukerji, T. & Dvorkin, J., 1998. *The Rock Physics Handbook,Tool for Seismic Analysis in Porous Media,* edn, Vol., pp. Pages, Cambridge University Press,U.K.

Mavko, G., Mukerji, T. & Dvorkin, J., 2003. *The Rock Physics Handbook,* edn, Vol., pp. Pages.

Mclaughlin, R., 1977. Study of Differential Scheme for Composite-Materials, *Int J Eng Sci,* 15**,** 237-244.

Meredith, D.J. & Egan, S.S., 2002. The geological and geodynamic evolution of the eastern Black Sea basin: insights from 2-D and 3-D tectonic modelling, *Tectonophysics,* 350**,** 157-179.

Milanovsky, E.E., Nikishin, A.M., Kopaevich, L.F., Gavrilov, O.Y. & Kluting, S., 1992. Correlation of Phases of Litospheric Plates Kinematics Reorganization and the World Ocean Short-Period Level Changes, *Doklady Akademii Nauk,* 326**,** 313-317.

Milton, G.W., 1985. The Coherent Potential Approximation Is a Realizable Effective Medium Scheme, *Commun Math Phys,* 99**,** 463-500.

Mindlin, R.D., 1949. Compliance of elastic bodies in Contact, *J.Appl.Mech.,* 16**,** 259-268.

Mukerji, T., Berryman, J., Mavko, G. & Berge, P., 1995. Differential Effective-Medium Modeling of Rock Elastic-Moduli with Critical Porosity Constraints, *Geophysical Research Letters,* 22**,** 555-558.

Muratov, M.V., 1972. Formation history of the deep Black Sea basin as compared with deep basins of the Medterranean., *Geotektonika,* 5**,** 22-41,in Russian.
Neuzil, C. E. (1995). Abnormal pressures as hydrodynamic phenomena.*American Journal of Science*, *295*(6), 742-786.
Nikishin, A. M., Cloetingh, S. A. P. L., Brunet, M. F., Stephenson, R. A., Bolotov, S. N., & Ershov, A. V. (1998). Scythian Platform, Caucasus and Black Sea region: Mesozoic-Cenozoic tectonic history and dymanics. *Mémoires du Muséum national d'histoire naturelle*, *177*, 163-176.
Nikishin, A.M., Ziegler, P.A., Panov, D.I., Nazarevich, B.P., Brunet, M.F., Stephenson, R.A., Bolotov, S.N., Korotaev, M.V. & Tikhomirov, P.L., 2001. Mesozoic and Cainozoic evolution of the Scythian Platform-Black Sea-Caucasus domain, *Peri-Tethys Memoir 6: Peri-Tethyan Rift/Wrench Basins and Passive Margins,* 186**,** 295-346
Nikishin, A. M., Ziegler, P. A., Abbott, D., Brunet, M. F., & Cloetingh, S. A. P. L. (2002). Permo–Triassic intraplate magmatism and rifting in Eurasia: implications for mantle plumes and mantle dynamics. *Tectonophysics*, *351*(1), 3-39.
Nikishin, A., 2003. The Black Sea basin: tectonic history and Neogene Quaternary rapid subsidence modelling, *Sedimentary Geology,* 156**,** 149-168.
Nikishin, A.M., Korotaev, M.V., Ershov, A.V. & Brunet, M.F., 2003. The Black Sea basin: tectonic history and Neogene-Quaternary rapid subsidence modelling, *Sedimentary Geology,* 156**,** 149-168.
Norris, A.N., 1985. A differential scheme for the effective moduli of composites, *Mechanics of Materials|Mechanics of Materials,* 4**,** 1-16.
Norris, A.N., Callegari, A.J. & Sheng, P., 1985. A GENERALIZED DIFFERENTIAL EFFECTIVE MEDIUM THEORY, *Journal of the Mechanics and Physics of Solids,* 33**,** 525-543.
Okay, A. I., & Sahinturk, O. (1997). AAPG Memoir 68: Regional and Petroleum Geology of the Black Sea and Surrounding Region. Chapter 15: Geology of the Eastern Pontides.
Okay, A.I., Sengor, A.M.C. & Gorur, N., 1994. Kinematic History of the Opening of the Black-Sea and Its Effect on the Surrounding Regions, *Geology,* 22**,** 267-270.
Osborne, M.J. & Swarbrick, R.E., 1997. Mechanisms for generating overpressure in sedimentary basins: A reevaluation, *Aapg Bulletin,* 81**,** 1023-1041.
Purnell, G.W., 1992. Imaging beneath a high-velocity layer using converted waves, *Geophysics,* 57**,** 1444-1452.
Robinson, A., Spadini, G., Cloetingh, S. & Rudat, J., 1995a. Stratigraphic Evolution of the Black-Sea - Inferences from Basin Modeling, *Marine and Petroleum Geology,* 12**,** 821-835.
Robinson, A.G., Banks, C.J., Rutherford, M.M. & Hirst, J.P.P., 1995b. Stratigraphic and Structural Development of the Eastern Pontides, Turkey, *Journal of the Geological Society,* 152**,** 861-872.
Robinson, A.G., Rudat, J.H., Banks, C.J. & Wiles, R.L.F., 1996. Petroleum geology of the Black Sea, *Marine and Petroleum Geology,* 13**,** 195-223.
Roscoe, R., 1952. The viscosity of suspensions of rigid spheres, *Br. J. Appl. Phys.,* 3**,** 267-269.
Ross, D.A., 1978. Summary of results of Black Sea drilling, *Initial reports DSDP,* 42**,** 1149-1177.

Rudat, J.H. & MacGregor, D.S., 1993. Uncoventional exploration techniques in a high cost deep water basin: A case study from the Black Sea., *Society of Exploratioal Geophysics,Abstr. Progr.*

Schon, J.H., 1996. *Physical Properties of rocks : Fundamentals and principles of petrophysics,* edn, Vol. 18, pp. Pages.

Scott, C.L., 2008. Formation and evolution of the eastern Black sea basin:Constraints from wide-angle seismc data,PhD thesis, Doctor of Philosophy, University of southampton, Southampton.

Scott, C.L., Shillington, D.J., Minshull, T.A., Edwards, R.A., Brown, P.J. & White, N.J., 2009. Wide-angle seismic data reveal extensive overpressures in the Eastern Black Sea Basin, *Geophysical Journal International,* 178**,** 1145-1163.

Screaton, E., Saffer, D., Henry, P. & Hunze, S., 2002. Porosity loss within the underthrust sediments of the Nankai accretionary complex: Implications for overpressures, *Geology,* 30**,** 19.

Shillington, D. J., White, N., Minshull, T. A., Edwards, G. R., Jones, S. M., Edwards, R. A., & Scott, C. L. (2008). Cenozoic evolution of the eastern Black Sea: A test of depth-dependent stretching models. *Earth and Planetary Science Letters*, *265*(3), 360-378.

Shillington, D.J., Scott, C.L., Minshull, T.A., Edwards, R.A., Brown, P.J. & White, N., 2009. Abrupt transition from magma-starved to magma-rich rifting in the eastern Black Sea, *Geology,* 37**,** 7-10.

Sorokin, Y. U. I. "The Black Sea." (1983).

Spadini, G., Robinson, A. & Cloetingh, S., 1996. Western versus Eastern Black Sea tectonic evolution: Pre-rift lithospheric controls on basin formation, *Tectonophysics,* 266**,** 139-154.

Spencer, C. W. (1987). Hydrocarbon generation as a mechanism for overpressuring in Rocky Mountain region. *AAPG bulletin*, *71*(4), 368-388.

Stewart, R.R., Gaiser, J.E., Brown, R.J. & Lawton, D.C., 2003. Converted-wave seismic exploration: Applications, *Geophysics,* 68**,** 40.

Swarbrick, R.E. & Osborne, M.J., 1998. Mechanisms that generate abnormal, pressures: An overview, *Abnormal Pressures in Hydrocarbon Environments,* 70**,** 13-34.

Tsuji, T., Tokuyama, H., Pisani, P. C., & Moore, G. (2008). Effective stress and pore pressure in the Nankai accretionary prism off the Muroto Peninsula, southwestern Japan. *Journal of Geophysical Research*, *113*(B11), B11401.

Wang, T. K., & Pan, C. H. (2001). Crustal Poisson's ratio off Eastern Taiwan from OBS data modeling. *TERRESTRIAL ATMOSPHERIC AND OCEANIC SCIENCES*, *12*(SUPP), 249-268.

Yonezawa, F. & Cohen, M.H., 1983. Granular Effective Medium Approximation, *Journal of Applied Physics,* 54**,** 2895-2899.

Zelt, C.A. & Smith, R.B., 1992. Seismic Traveltime Inversion for 2-D Crustal Velocity Structure, *Geophysical Journal International,* 108**,** 16-34.

Zonenshain, L.P. & Lepichon, X., 1986. Deep Basins of the Black-Sea and Caspian Sea as Remnants of Mesozoic Back-Arc Basins, *Tectonophysics,* 123**,** 181-211.